arXiv:1407.3451v3 [astro-ph.CO] 24 Sep 2014

To appear in *The Astrophysical Journal*

ELUCID - Exploring the Local Universe with reConstructed Initial Density field I: Hamiltonian Markov Chain Monte Carlo Method with Particle Mesh Dynamics

Huiyuan Wang[1,2], H.J. Mo[1,2], Xiaohu Yang[3,4], Y. P. Jing[4] and W. P. Lin[3]

ABSTRACT

Simulating the evolution of the local universe is important for studying galaxies and the intergalactic medium in a way free of cosmic variance. Here we present a method to reconstruct the initial linear density field from an input non-linear density field, employing the Hamiltonian Markov Chain Monte Carlo (HMC) algorithm combined with Particle Mesh (PM) dynamics. The HMC+PM method is applied to cosmological simulations, and the reconstructed linear density fields are then evolved to the present day with N-body simulations. The constrained simulations so obtained accurately reproduce both the amplitudes and phases of the input simulations at various z. Using a PM model with a grid cell size of $0.75\,h^{-1}$Mpc and 40 time-steps in the HMC can recover more than half of the phase information down to a scale $k \sim 0.85\,h\mathrm{Mpc}^{-1}$ at high z and to $k \sim 3.4\,h\mathrm{Mpc}^{-1}$ at $z = 0$, which represents a significant improvement over similar reconstruction models in the literature, and indicates that our model can reconstruct the formation histories of cosmic structures over a large dynamical range. Adopting PM models with higher spatial and temporal resolutions yields even better reconstructions, suggesting that our method is limited more by the availability of computer resource than by principle. Dynamic models of structure evolution adopted in many earlier investigations can induce non-Gaussianity in the reconstructed linear density field, which in turn can cause large systematic deviations in the predicted halo mass function. Such deviations are greatly reduced or absent in our reconstruction.

Subject headings: dark matter - large-scale structure of the universe - galaxies: haloes - methods: statistical

[1]Key Laboratory for Research in Galaxies and Cosmology, Department of Astronomy, University of Science and Technology of China, Hefei, Anhui 230026, China; whywang@mail.ustc.edu.cn

[2]Department of Astronomy, University of Massachusetts, Amherst MA 01003-9305, USA

[3]Key Laboratory for Research in Galaxies and Cosmology, Shanghai Astronomical Observatory, Shanghai 200030, China

[4]Center for Astronomy and Astrophysics, Shanghai Jiao Tong University, Shanghai 200240, China

1. Introduction

A key step in understanding the physical processes of galaxy formation is to investigate the correlations and interactions among galaxies, baryonic gas [particularly interstellar media and intergalactic media (IGM)] and dark matter. Many observational programs have been carried out for galaxies and the gas components. Large redshift surveys, such as the Sloan Digital Sky Survey (SDSS; York et al. 2000), can now provide a huge amount of information about the intrinsic properties of galaxies and their clustering in space. Interstellar gas closely associated with galaxies can be observed through its 21cm emission of neutral hydrogen gas (e.g. Koribalski et al. 2004; Springob et al. 2005; Giovanelli et al. 2005), and through millimeter/submillimeter emissions of molecular gas (e.g. Young et al. 1995; Saintonge et al. 2011). The diffuse cold/warm components in the IGM can be studied using quasar absorption line systems (e.g. Savage, Tripp, & Lu 1998; Fang et al. 2002; Werk et al. 2013), while the hot components can be studied through X-ray observations and through their Sunyaev-Zel'dovich effect in the Cosmic Microwave Background (see Carlstrom, Holder, & Reese 2002, for a review).

In order to make full use of the potential of these observational data, one has to develop optimal strategies. Clearly, it is important to have as much constraints on the dark matter component. As the dominating mass component of the cosmic density field, the distribution of dark matter relative to the galaxy population and the IGM can provide important information about the large-scale environments within which galaxies and the gas components evolve. In particular, any constraints on the evolutionary histories of the dark matter structures within which the observed galaxies and gas reside can provide direct information on how the interactions between the dark matter and baryonic components shape the observed properties of galaxies and IGM.

Unfortunately, the details about the distribution and evolution of the dark matter component in the observed universe is not directly available; current observations of gravitational lensing can only provide constraints on the properties of the mass density field in a statistical way but not on an object-to-object basis. One promising way to make progress in this direction is to reconstruct the initial (linear) density field from which the observed structures in the present-day universe form. This is now possible owing to the well established paradigm, the ΛCDM model, within which the relationship between galaxy systems (individual galaxies, groups and clusters of galaxies) and the underlying dark matter distribution can be modeled quite accurately through the connection between the distribution of dark matter halos and the overall mass distribution. With such reconstructed initial conditions, one can use high-resolution numerical simulations (usually referred to as constrained simulations) to reproduce the time evolution of the density field in the local Universe. This can not only be used to trace the present-day environments in which observed galaxies reside, but also provide the formation histories of individual structures to understand the interaction between dark matter and baryonic components. Indeed, together with galaxy formation and baryonic physics, the reconstructed initial conditions allow one to simulate the formation and evolution of the galaxy population and IGM in the local Universe. Such an approach is particularly powerful in constraining theory with observation, because many observations, such as those for

dwarf galaxies and for low-z quasar absorption line systems, can only be carried out in relatively small volumes, and so the cosmic variance is usually a big issue. The uncertainties due to the cosmic variance can be minimized by making comparisons between observations and model predictions for systems that have both the same environments and the same formation histories, which is exactly an accurate constrained simulation is capable of doing.

Numerous attempts have been made to develop methods to reconstruct the initial conditions of structure formation in the local universe using galaxy distributions and/or peculiar velocities. Hoffman & Ribak (1991) developed a method to construct Gaussian random fields that are subjected to various constraints (see also Bertschinger 1987; van de Weygaert & Bertschinger 1996; Klypin et al. 2003; Kitaura & Enßlin 2008). Klypin et al. (2003) improved this method by using Wiener Filter (see e.g. Zaroubi et al. 1995) to deal with sparse and noisy data. Gaussian density fields constrained by the peculiar velocities of galaxies in the local universe have been used to set up the initial conditions for constrained simulations (e.g. Kravtsov, Klypin, & Hoffman 2002; Klypin et al. 2003; Gottloeber, Hoffman, & Yepes 2010). Note, however, that the basic underlying assumption in this method is that the linear theory is valid on all scales (Klypin et al. 2003; Doumler et al. 2013).

Nusser & Dekel (1992) proposed a method which employs quasi-linear dynamics for structure evolution. This method traces the non-linear mass (galaxy) density field back in time to the linear regime according to the Zel'dovich approximation in Eulerian space (see Peebles 1989, for another related approach). Under the assumption of the absence of multi-streaming (shell-crossing), Brenier et al. (2003) found that the reconstruction problem can be treated as an instance of optimal mass transportation, and developed a Monge-Ampére-Kantorovich (MKA) method to recover the particle displacement field (see also Frisch et al. 2002). These two methods are valid only on scales where a one-to-one relation between the Lagrangian and Eulerian coordinates exists. Furthermore the two methods did not take account of any priors about the statistical properties of the initial density field, and so the reconstructed initial density field is not guaranteed to be Gaussian (Kolatt et al. 1996; Doumler et al. 2013).

In order to achieve a high reconstruction precision and simultaneously to avoid non-Gaussianity, several hybrid approaches have been proposed. For example, Lavaux (2010) used the MKA method to generate constraints from observations, requiring the constraints to have Gaussian distributions. Doumler et al. (2013) extended the method by adding an inverse Zel'dovich approximation.

More recently, Bayesian approaches have been proposed, in which the initial (linear) density field is sampled from a posterior probability distribution function consisting of a Gaussian prior and a likelihood (Jasche & Wandelt 2013; Kitaura 2013; Wang et al. 2013; Heß, Kitaura, & Gottlöber 2013). In such an approach, a specific dynamic model of structure evolution has to be adopted to link the linear density field to the observed galaxy distribution (e.g. Jasche & Wandelt 2013; Kitaura 2013) or to the present-day mass density field inferred from other means (Wang et al. 2013, hereafter W13). The models used in the literature include the modified Zel'dovich approximation

(MZA, Tassev & Zaldarriaga 2012b, hereafter TZ12), the second order Lagrangian perturbation theory (2LPT), and the augmented Lagrangian perturbation theory (ALPT, Kitaura & Heß 2013). In such a Bayesian approach, different initial density fields are evolved forward to predict the non-linear density field today, and their merits are evaluated in terms of adopted priors and how well their predicted non-linear density fields match the constraining input field (Jasche & Wandelt 2013). The advantage of such an approach is twofold. First, it automatically takes into account priors for the initial density field. Second, as a 'forward' approach, it is not limited by the development of multi-stream flows, as long as the adopted dynamical model can follow them accurately.

Clearly, the performance of the Bayesian approach depends on the accuracy of the dynamical model adopted to follow the structure evolution. As to be detailed in Section 6, the dynamical models so far adopted work only accurately at wave-numbers $k \lesssim 0.5\,h\mathrm{Mpc}^{-1}$, i.e. only in the quasi-nonlinear regime. They can not properly account for the evolution of highly non-linear structures, such as massive clusters, filaments and sheets, where shell-crossing is frequent. If such an approximate model is adopted to reconstruct the structures in the non-linear regime, bias can be introduced into the reconstructed initial conditions. Such bias sometimes can be very significant and may greatly reduce the usefulness of the reconstructed initial density field.

In this first paper of a series, we develop a method combining the Bayesian reconstruction approach with a much more accurate dynamic model of structure evolution, the Particle Mesh (PM) model. The PM technique has been commonly adopted in N-body codes to evaluate gravitational forces on relatively large scales (see e.g. White, Frenk, & Davis 1983; Klypin & Shandarin 1983; Jing & Suto 2002; Springel 2005), and can follow the structure evolution accurately as long as the grid cells and time steps are chosen sufficiently small. We show that our method is limited more by the availability of computer resource than by principle. Even with a modest computer resource, the reconstruction accuracy our method can achieve is already much higher than those of the other methods in the literature.

The structure of the paper is organized as follows. In Section 2, we describe our reconstruction method based on Hamiltonian Markov Chain Monte Carlo (hereafter HMC). Section 3 describes the N-body simulations used for testing our method, and how the quality of the PM model depends on model parameters. In Section 4, we test our HMC+PM method by applying it to high-resolution numerical simulations. In Section 5, we use N-body simulations to follow the structure evolution seeded by the reconstructed linear density field and compare the results with the original simulations to examine various aspect of our method. Section 6 shows the comparison between the results of HMC reconstructions adopting different dynamical models. Finally, in Section 7 we summarize our main results and make some further discussions. Many abbreviations, terms and quantities are used in the text. To avoid confusion, we provide a list of them together with their definitions in Appendix A.

2. The reconstruction method

Our objective is to reconstruct the linear (or initial) density field from an input non-linear density field, $\rho_{\rm inp}(\mathbf{x})$, at low redshift, such as at the present day. The input density field can either be that from an accurate cosmological simulation ($\rho_{\rm si}$), as is the case here for testing the method of reconstruction, or that reconstructed from observations, such as a galaxy redshift survey that can be used to trace the current mass density field in the Universe. There are two constraints on this linear density field, which can be specified by its Fourier transform, $\delta(\mathbf{k})$. First, the linear density field is required to be consistent with a chosen cosmology. We assume the standard ΛCDM model, and so the linear density field obeys a Gaussian distribution with variance given by the linear power spectrum, $P_{\rm lin}(k)$. Second, the modeled density field, $\rho_{\rm mod}(\mathbf{x})$, evolved from $\delta(\mathbf{k})$ according to a chosen dynamical model of structure evolution, should match the input density field, $\rho_{\rm inp}(\mathbf{x})$, as close as possible.

Owing to the complexity of the problem, such as the very high dimensionality of the parameter space, and the uncertainty and incompleteness in the constraining field, $\rho_{\rm inp}(\mathbf{x})$, the solution may not be unique. We therefore follow W13 and construct a posterior probability distribution for $\delta(\mathbf{k})$ given $\rho_{\rm inp}(\mathbf{x})$ as

$$\begin{aligned} Q(\delta_j(\mathbf{k})|\rho_{\rm inp}(\mathbf{x})) &= {\rm e}^{-\chi^2} \times G(\delta(\mathbf{k})) \\ &= {\rm e}^{-\sum_{\mathbf{x}}[\rho_{\rm mod}(\mathbf{x})-\rho_{\rm inp}(\mathbf{x})]^2\omega(\mathbf{x})/2\sigma^2_{\rm inp}(\mathbf{x})} \times \prod_{\mathbf{k}}^{\rm half}\prod_{j={\rm re}}^{\rm im} \frac{1}{[\pi P_{\rm lin}(k)]^{1/2}} {\rm e}^{-[\delta_j(\mathbf{k})]^2/P_{\rm lin}(k)}, \quad (1) \end{aligned}$$

where $\sigma_{\rm inp}$ is the statistical uncertainties in $\rho_{\rm inp}$, while $\omega(\mathbf{x})$ is a weight function used to account for possible incompleteness. The subscripts $j = {\rm re}, {\rm im}$ denote the real and imaginary parts, respectively. Since $\delta(\mathbf{k})$ is the Fourier transform of a real field, we have $\delta(\mathbf{k}) = \delta^*(-\mathbf{k})$ so that only the Fourier modes in the upper half-space are needed. All these fields are to be sampled in a periodic box of length L on a side, divided into $N_{\rm c}$ grid cells in each dimension. The term, $G(\delta(\mathbf{k}))$, in the equation represents the first constraint mentioned above, i.e. the prior Gaussian distribution of $\delta(\mathbf{k})$, while the ${\rm e}^{-\chi^2}$ term accounts for the second constraint and can be regarded as the likelihood for $\rho_{\rm mod}(\mathbf{x})$ given $\rho_{\rm inp}(\mathbf{x})$.

Our purpose is thus to seek the solutions of $\delta(\mathbf{k})$ that maximize the posterior probability distribution function $Q(\delta_j(\mathbf{k})|\rho_{\rm inp}(\mathbf{x}))$. As demonstrated in W13, the Hamiltonian Markov Chain Monte Carlo (HMC) technique developed by Duane et al. (1987) and Neal (1996) can help us to achieve this goal, as it can sample a posterior distribution in a large, multi-dimensional parameter space very efficiently (Hanson 2001). This method has been widely applied in astrophysics and cosmology (e.g. Hajian 2007; Taylor, Ashdown, & Hobson 2008; Jasche & Kitaura 2010; Kitaura, Gallerani, & Ferrara 2012; Jasche & Wandelt 2013; Kitaura 2013; Wang et al. 2013; Heß, Kitaura, & Gottlöber 2013). In particular, Jasche & Wandelt (2013), Kitaura (2013), W13 and Heß, Kitaura, & Gottlöber (2013) adopted this technique to reconstruct the initial conditions for the local universe. A brief description about the method is given in Section 2.1.

In order to predict $\rho_{\rm mod}(\mathbf{x})$ from $\delta(\mathbf{k})$, a structure formation model is required to evolve the cosmic density field. In this paper, we first use the Zel'dovich approximation to generate the particle distribution at a given high redshift, and then use the Particle-Mesh (PM) model to evolve the cosmic density field traced by these particles. These techniques are well developed and have been adopted in many cosmological simulations (Zel'dovich 1970; White, Frenk, & Davis 1983; Klypin & Shandarin 1983; Jing & Suto 2002; Springel 2005). In Section 2.2 we provide key equations used in our reconstruction. Because the HMC method utilizes the gradients, $\partial\rho_{\rm mod}(\mathbf{x})/\partial\delta_{\rm j}(\mathbf{k})$, to suppress random walks in the MCMC implementation and to improve the efficiency, it is necessary to obtain these gradients from the adopted dynamic model for structure evolution. The derivation of the Hamiltonian force, which is the combination of these gradients, is described in Section 2.3 and in Appendix B.

2.1. The Hamiltonian Markov Chain Monte Carlo Algorithm

The algorithm is designed to sample the posterior distribution (our target distribution) in a way analogous to solving a physical system in Hamiltonian dynamics. The 'potential' of the system is defined as the negative of the natural logarithm of the target distribution,

$$\psi[\delta_j(\mathbf{k})] \equiv -\ln(Q) = \sum_{\mathbf{k}}^{\rm half} \ln[\pi P_{\rm lin}(k)] + \sum_{\mathbf{k}}^{\rm half}\sum_{j={\rm re}}^{\rm im} \frac{[\delta_j(\mathbf{k})]^2}{P_{\rm lin}(k)} + \sum_{\mathbf{x}} \frac{[\rho_{\rm mod}(\mathbf{x}) - \rho_{\rm inp}(\mathbf{x})]^2\omega(\mathbf{x})}{2\sigma^2_{\rm inp}(\mathbf{x})}\,. \quad (2)$$

For each $\delta_j(\mathbf{k})$, a momentum variable, $p_j(\mathbf{k})$, is introduced and the Hamiltonian of the system is constructed as

$$H = \sum_{\mathbf{k}}^{\rm half}\sum_{j={\rm re}}^{\rm im} \frac{p_j^2(\mathbf{k})}{2m_j(\mathbf{k})} + \psi[\delta_j(\mathbf{k})]\,, \quad (3)$$

where $m_j(\mathbf{k})$ is a fictitious mass.

The statistical properties of the system is characterized by the partition function, $\exp(-H)$, which is separated into a Gaussian distribution in the momenta $p_j(\mathbf{k})$ multiplied by the target distribution:

$$\exp(-H) = Q[\delta_j(\mathbf{k})|\rho_{\rm p}(\mathbf{x})] \prod_{\mathbf{k}}^{\rm half}\prod_{j={\rm re}}^{\rm im} {\rm e}^{-\frac{p_j^2(\mathbf{k})}{2m_j(\mathbf{k})}}\,. \quad (4)$$

As can be seen, the target distribution can be obtained by sampling this partition function and then marginalizing over the momenta.

In order to sample the distribution, we first pick a set of momenta $p_j(\mathbf{k})$ randomly from the multi-dimensional, un-correlated Gaussian distribution with variances $m_j(\mathbf{k})$. We then evolve the system from the starting point, $[\delta_j(\mathbf{k}), p_j(\mathbf{k})]$, according to the Hamilton equations. In practice, the leapfrog technique is adopted to integrate the "equations of motion":

$$p_j(\mathbf{k}, t+\tau/2) = p_j(\mathbf{k}, t) - \frac{\tau}{2}\frac{\partial H}{\partial\delta_j(\mathbf{k})}\bigg|_t\,; \quad (5)$$

$$\delta_j(\mathbf{k}, t+\tau) = \delta_j(\mathbf{k}, t) + \frac{\tau}{m_j(\mathbf{k})} p_j(\mathbf{k}, t+\tau/2)\,; \tag{6}$$

$$p_j(\mathbf{k}, t+\tau) = p_j(\mathbf{k}, t+\tau/2) - \frac{\tau}{2}\frac{\partial H}{\partial \delta_j(\mathbf{k})}\bigg|_{t+\tau}\,, \tag{7}$$

where τ is the time increment for the leapfrog step. The equations are integrated for n leapfrog steps (referred to as one chain step) to a final point, $[\delta_j'(\mathbf{k}), p_j'(\mathbf{k})]$, in phase space. This final state is accepted with a probability

$$p = \min\left\{1, \mathrm{e}^{-[H(\delta_j'(\mathbf{k}), p_j'(\mathbf{k})) - H(\delta_j(\mathbf{k}), p_j(\mathbf{k}))]}\right\}\,. \tag{8}$$

Since the Hamiltonian of a physical system is conserved, the acceptance rate should in principle be unity, which is one of the main advantages of the HMC method. In practice, however, rejection can occur because of numerical errors. The above process is repeated by randomly picking a new set of momenta.

As one can see from equations (5) - (7), the Hamiltonian force, $\partial H/\partial\delta_j(\mathbf{k})$, is the most important quantity to compute in order to evolve the system forward in t. Combining equation (2) and (3), we can write

$$\frac{\partial H}{\partial \delta_j(\mathbf{k})} = \frac{2\delta_j(\mathbf{k})}{P_{\rm lin}(k)} + \frac{\partial \chi^2}{\partial \delta_j(\mathbf{k})} = \frac{2\delta_j(\mathbf{k})}{P_{\rm lin}(k)} + F_j(\mathbf{k})\,, \tag{9}$$

where

$$F_j(\mathbf{k}) \equiv \frac{\partial \chi^2}{\partial \delta_j(\mathbf{k})} \tag{10}$$

is the likelihood term of the Hamiltonian force to be discussed in great detail in Section 2.3 and in Appendix B. In order to proceed, two other parameters, the Hamiltonian mass $m_j(\mathbf{k})$ and the pseudo time $T = n\tau$, have to be specified. As shown in Hanson (2001), these two parameters have to be chosen carefully, because they can affect the sampling efficiency significantly. To avoid resonant trajectory, T must be randomized. We thus randomly pick n and τ from two uniform distributions in the range of $[1, n_{\rm max}]$ and $[0, \tau_{\rm max}]$, respectively. Following W13, we set $n_{\rm max} = 13$ and $\tau_{\rm max} \sim 0.1$ and define the Hamiltonian mass as,

$$m_j(\mathbf{k}) \equiv m(k) = \frac{2}{P_{\rm lin}(k)} + \sqrt{\frac{\sum_{j=\rm re}^{\rm im}\langle F_j^2(\mathbf{k})\rangle_{\mathbf{k}}}{P_{\rm lin}(k)}}\,, \tag{11}$$

where $\langle\cdots\rangle_{\mathbf{k}}$ represents average over the phase of $\mathbf{k}$. The suitability of this mass definition is detailed in W13.

2.2. Dynamic Model of Structure Evolution

In this section, we describe the dynamic model of structure evolution adopted here to link the final density field, $\rho_{\rm mod}(\mathbf{x})$, with the initial linear density field, $\delta(\mathbf{k})$. We first use the Zel'dovich

approximation to generate the positions and velocities of particles at a given initial redshift $z_{\rm i}$ based on the linear density field $\delta(\mathbf{k})$. We then use the Particle-Mesh (PM) technique to evolve the initial density field to the present day to obtain $\rho_{\rm mod}(\mathbf{x})$.

2.2.1. The Zel'dovich Approximation

For a particle with Lagrangian position $\mathbf{q}$, we use the Zel'dovich approximation to derive its position $\mathbf{r}_{\rm i}(\mathbf{q})$ and velocity $\mathbf{v}_{\rm i}(\mathbf{q})$ at initial redshift $z_{\rm i}$ as,

$$\mathbf{r}_{\rm i}(\mathbf{q}) = \mathbf{q} + \mathbf{s}(\mathbf{q})\,; \tag{12}$$

$$\mathbf{v}_{\rm i}(\mathbf{q}) = H_{\rm i} a_{\rm i}^2 f(\Omega_{\rm i})\mathbf{s}(\mathbf{q})\,. \tag{13}$$

Here, $H_{\rm i}$ is the Hubble constant at $z_{\rm i}$; $a_{\rm i} = 1/(1+z_{\rm i})$ is the scale factor; and $f(\Omega) = {\rm d}\ln D/{\rm d}\ln a$ with $D(a)$ the linear growth factor. The Fourier transform of the displacement field $\mathbf{s}(\mathbf{q})$ is given by

$$\mathbf{s}(\mathbf{k}) = \frac{i\mathbf{k}}{k^2} D(a_{\rm i})\delta(\mathbf{k})\,. \tag{14}$$

Note that the particle velocities $\mathbf{v}(\mathbf{q})$ are not the peculiar velocities; the peculiar velocities are $\mathbf{u} = \mathbf{v}(\mathbf{q})/a$. This definition of velocity allows us to get rid of the $\dot{a}/a$ terms in the equations of motion to be shown in the following. We use $\mathbf{x}$ to indicate the position of a grid cell, and $\mathbf{q}$ and $\mathbf{r}$ to denote the Lagrangian and Eulerian coordinates of a particle, respectively, all in co-moving units. Both $\mathbf{x}$ and $\mathbf{q}$ are regularly spaced, while $\mathbf{r}$ is not.

2.2.2. The Particle-Mesh Model

Under gravitational interaction, the equations of motion for the mass particles set up above can be written as

$$\frac{{\rm d}\mathbf{r}}{{\rm d}a} = \frac{1}{a^2\dot{a}}\mathbf{v}\,; \tag{15}$$

$$\frac{{\rm d}\mathbf{v}}{{\rm d}a} = -\frac{4\pi G\bar{\rho}_0}{a\dot{a}}\nabla\Phi\,, \tag{16}$$

where $\bar{\rho}_0$ is the mean mass density of the Universe at $z = 0$. Note again that $\mathbf{v} = a\mathbf{u}$ with $\mathbf{u} = a{\rm d}\mathbf{r}/{\rm d}t$. The gravitational potential Φ can be obtained by solving the Poisson equation,

$$\nabla^2\Phi = \delta(a, \mathbf{r})\,, \tag{17}$$

where $\delta(a, \mathbf{r})$ is the overdensity field at $z = 1/a - 1$.

In practice, we use the leapfrog technique to integrate the above equations forward in time (or in a):

$$\mathbf{v}(\mathbf{q}, a_{n+1/2}) = \mathbf{v}(\mathbf{q}, a_{n-1/2}) - \nabla\Phi(\mathbf{r}(\mathbf{q}, a_n)) \int_{a_{n-1/2}}^{a_{n+1/2}} \frac{4\pi G\bar{\rho}_0}{a\dot{a}}{\rm d}a\,; \tag{18}$$

$$\mathbf{r}(\mathbf{q}, a_{n+1}) = \mathbf{r}(\mathbf{q}, a_n) + \mathbf{v}(\mathbf{q}, a_{n+1/2}) \int_{a_n}^{a_{n+1}} \frac{1}{a^2 \dot{a}} \mathrm{d}a \,. \tag{19}$$

For the sake of simplicity, we rewrite these two equations as

$$\mathbf{v}_{n+1/2}(\mathbf{q}) = \mathbf{v}_{n-1/2}(\mathbf{q}) + \mathbf{F}_n(\mathbf{r}_n(\mathbf{q}))\Delta_n^{\rm v} \,; \tag{20}$$

$$\mathbf{r}_{n+1}(\mathbf{q}) = \mathbf{r}_n(\mathbf{q}) + \mathbf{v}_{n+1/2}(\mathbf{q})\Delta_n^{\rm r} = \mathbf{r}_n(\mathbf{q}) + \mathbf{v}_{n-1/2}(\mathbf{q})\Delta_n^{\rm r} + \mathbf{F}_n(\mathbf{r}_n(\mathbf{q}))\Delta_n^{\rm v}\Delta_n^{\rm r} \,, \tag{21}$$

where $\Delta_n^{\rm v}$ and $\Delta_n^{\rm r}$ are the integrations in equations (18) and (19), respectively; n is the step number; and $a_{n+1/2} = (a_n + a_{n+1})/2$.

We adopt the standard procedure to calculate the gravitational force, $\mathbf{F}_n(\mathbf{r}_n(\mathbf{q}))$ (e.g. Springel 2005). After obtaining the positions of all mass particles at the nth leapfrog step, $\mathbf{r}_n(\mathbf{q}_2)$, we use a clouds-in-cells (CIC) assignment (Hockney & Eastwood 1981) to construct the overdensity field on a grid:

$$\delta_{n,\rm c}(\mathbf{x}_2) = \sum_{\mathbf{q}_2} w_{\rm c}(\mathbf{x}_2 - \mathbf{r}_n(\mathbf{q}_2)) - 1 \,, \tag{22}$$

where $w_{\rm c}(\mathbf{x}_2 - \mathbf{r}_n(\mathbf{q}_2))$ is the CIC kernel in real space. We Fourier transform the density field and divide it by the CIC kernel in Fourier space, $w_{\rm c}(\mathbf{k}) = {\rm sinc}(k_x L/2N_{\rm c}){\rm sinc}(k_y L/2N_{\rm c}){\rm sinc}(k_z L/2N_{\rm c})$, to correct for the smoothing effect of the CIC assignment. The resulting density field is convolved with a Gaussian kernel $w_{\rm g}(R_{\rm PM}k)$ to suppress the force anisotropy that may be produced by the finite size of grid cells. Here $R_{\rm PM}$ is fixed to be $1.2l_c$, with $l_c = L/N_{\rm c}$ the grid cell size. The smoothed density field at the nth step can then be written as,

$$\delta_n(\mathbf{k}) = \frac{w_{\rm g}(R_{\rm PM}k)}{w_{\rm c}(\mathbf{k})N_{\rm c}^3} \sum_{\mathbf{x}_2} {\rm e}^{-i\mathbf{k}\cdot\mathbf{x}_2} \delta_{n,\rm c}(\mathbf{x}_2) \,. \tag{23}$$

Multiplying $\delta_n(\mathbf{k})$ with the Green function, $-1/k^2$, and with $-i\mathbf{k}$, we obtain the gravity in Fourier space. To obtain accurate forces at particle positions, we first divide the gravitational force in Fourier space by $w_{\rm c}(\mathbf{k})$, and then transform it back onto the real space grid:

$$\mathbf{F}_{{\rm g},n}(\mathbf{x}_1) = \sum_{\mathbf{k}} {\rm e}^{i\mathbf{k}\cdot\mathbf{x}_1} \frac{i\mathbf{k}}{k^2} \frac{w_{\rm g}(R_{\rm PM}k)}{w_{\rm c}^2(\mathbf{k})N_c^3} \sum_{\mathbf{x}_2} \delta_{n,\rm c}(\mathbf{x}_2){\rm e}^{-i\mathbf{k}\cdot\mathbf{x}_2} \,. \tag{24}$$

We interpolate the forces to particle positions using a CIC interpolation. Note that the smoothing introduced by the CIC interpolation has already been de-convolved before the Fourier transformation. Finally, the gravitational force at a given particle position can be expressed as

$$\mathbf{F}_n(\mathbf{r}_n(\mathbf{q}_1)) = \sum_{\mathbf{x}_1} \mathbf{F}_{{\rm g},n}(\mathbf{x}_1) w_{\rm c}(\mathbf{x}_1 - \mathbf{r}_n(\mathbf{q}_1)) \,. \tag{25}$$

After $N \equiv N_{\rm PM}$ steps,[1] we obtain the final particle positions, $\mathbf{r}_N(\mathbf{q}_1)$, at $z = 0$. The final density field is obtained using the same CIC assignment as described above:

$$\rho_{N,\rm c}(\mathbf{x}) = \sum_{\mathbf{q}_1} w_{\rm c}(\mathbf{x} - \mathbf{r}_N(\mathbf{q}_1)) \,. \tag{26}$$

[1]For conciseness, we will use N to replace $N_{\rm PM}$ in this and the next subsections, and in Appendix B.

This density field can not yet be used as our final modeled density field. Although the PM model used here is much more accurate than many perturbation theories adopted before, such as the Zel'dovich approximation and the 2LPT, the accuracy of the PM result depends on the number of steps adopted, in the sense that a larger $N_{\rm PM}$ leads to more accurate results. In practice, however, the value $N_{\rm PM}$ cannot be chosen to be much larger than 10 in order to complete the HMC within a reasonable computational time scale. The use of a relatively small $N_{\rm PM}$ can lead to significant bias in the PM density field relative to the real density field obtained from a high-resolution simulation. Fortunately, this bias can be corrected, at least partly. Following TZ12, we introduce a density transfer function between the modeled and real density fields,

$$T(k) = \frac{\langle \rho_{N,\rm c}(\mathbf{k})\rho^*_{\rm si}(\mathbf{k})\rangle_{\mathbf{k}}}{\langle \rho_{N,\rm c}(\mathbf{k})\rho^*_{N,\rm c}(\mathbf{k})\rangle_{\mathbf{k}}}\,, \tag{27}$$

where $\rho_{\rm si}$ is the $z = 0$ density field evolved from the same initial condition as $\rho_{N,\rm c}$ by using an accurate N-body code, here used to represent the real density field. As demonstrated in TZ12, the density transfer function has small variance among different realizations (see also Section 3.2), and so it is sufficient to estimate it only once. The final model prediction of the density field we actually use is, in Fourier space, given by

$$\rho_{\rm mod}(\mathbf{k}) = \frac{w_{\rm g}(R_{\rm s}k)T(k)}{w_{\rm c}(\mathbf{k})N_{\rm c}^3}\sum_{\mathbf{x}}\rho_{N,\rm c}(\mathbf{x})\mathrm{e}^{-i\mathbf{k}\cdot\mathbf{x}}\,. \tag{28}$$

Note that a new smoothing specified by $R_{\rm s}$, which is different from $R_{\rm PM}$ used in the PM model, is introduced here to suppress the shot noise in Hamiltonian force calculation, and to smooth out the difference between the modeled and simulated density fields on small scales produced by the inaccuracy of the dynamic model adopted in the HMC (see Section 3.2 for details).

2.3. The Likelihood Term of the Hamiltonian Force

As shown in equation (9), the Hamiltonian force consists of two components, the prior term, $2\delta_j(\mathbf{k})/P_{\rm lin}(k)$, and the likelihood term, $F_j(\mathbf{k})$. In our model the calculation of the likelihood (χ^2) term consists of three transformations. The first is the transformation of $\delta_j(\mathbf{k})$ to the initial positions and velocities, $\mathbf{p}_{\rm i}(\mathbf{q}) = [\mathbf{r}_{\rm i}(\mathbf{q}), \mathbf{v}_{\rm i}(\mathbf{q})]$, through the Zel'dovich approximation. The second is the transformation of the initial positions and velocities set up by the Zel'dovich approximation to the final positions and velocities $\mathbf{p}_N(\mathbf{q}) = [\mathbf{r}_N(\mathbf{q}), \mathbf{v}_{N-1/2}(\mathbf{q})]$ via $N \equiv N_{\rm PM}$ steps of the PM model.[2] In the following, we use $\mathbf{p}_n(\mathbf{q}) = [\mathbf{r}_n(\mathbf{q}), \mathbf{v}_{n-1/2}(\mathbf{q})]$ $(n = 1, 2, ..., N)$ to indicate the positions and velocities of particles at the nth PM step. Sometimes we also use $\mathbf{p}_0(\mathbf{q}) = [\mathbf{r}_0(\mathbf{q}), \mathbf{v}_0(\mathbf{q})]$ to indicate the initial condition, i.e. $\mathbf{p}_{\rm i}(\mathbf{q})$. The third one is the transformation of the final positions to the χ^2.

[2]It is not necessary to obtain $\mathbf{v}_N(\mathbf{q})$ because the velocities are not used in computing $\rho_{\rm mod}$ and χ^2.

The chain rule of differentiation allows us to rewrite the derivatives of χ^2 with respect to $\delta_j(\mathbf{k})$ as

$$F_j(\mathbf{k}) = \frac{\partial \chi^2}{\partial \delta_j(\mathbf{k})} = \frac{\partial \chi^2}{\partial \mathbf{p}_N} \otimes \frac{\partial \mathbf{p}_N}{\partial \mathbf{p}_{N-1}} \otimes \cdots \otimes \frac{\partial \mathbf{p}_2}{\partial \mathbf{p}_1} \otimes \frac{\partial \mathbf{p}_1}{\partial \mathbf{p}_0} \otimes \frac{\partial \mathbf{p}_0}{\partial \delta_j(\mathbf{k})} \,. \tag{29}$$

Here $\partial \mathbf{p}_{n+1}/\partial \mathbf{p}_n$ $(n = \mathrm{i}, 1, 2, \cdots, N-1)$ is a 6×6 (three coordinates and three components of velocity), $\partial \chi^2/\partial \mathbf{p}_N$ a 1×6, and $\partial \mathbf{p}_0/\partial \delta_j(\mathbf{k})$ a 6×1 matrix, and $\otimes$ denotes matrix multiplication.

As suggested by Hanson & Cunningham (1996), the matrix multiplications in the above equation can be carried out in two different ways. The first proceeds in the same time sequence as the structure formation, corresponding to the inverse order of the right hand side of equation (29). Namely one first calculates $\partial \mathbf{p}_0/\partial \delta_j(\mathbf{k})$, then $\partial \mathbf{p}_1/\partial \delta_j(\mathbf{k})$, and so on to $\partial \mathbf{p}_{N_{\rm PM}}/\partial \delta_j(\mathbf{k})$, and eventually obtaining $\partial \chi^2/\partial \delta_j(\mathbf{k})$. However, calculation along this sequence results in very large intermediate matrices – for example $\partial \mathbf{p}_0/\partial \delta_j(\mathbf{k})$ has $N_{\rm c}^6$ variables, and is almost impossible to handle. The second way proceeds in the opposite direction. One first calculates $\partial \chi^2/\partial \mathbf{p}_N$, then $\partial \chi^2/\partial \mathbf{p}_{N-1}$, and so on to $\partial \chi^2/\partial \mathbf{p}_0$ (which by definition is equal to $\partial \chi^2/\partial \mathbf{p}_{\rm i}$), eventually obtaining $\partial \chi^2/\partial \delta_j(\mathbf{k})$. This technique is called the adjoint differentiation technique by Hanson & Cunningham (1996).

In this order the calculation of the likelihood term of the Hamiltonian force consists of the following three parts. The first is the χ^2 transformation, which calculates $\partial \chi^2/\partial \mathbf{r}_N(\mathbf{q})$ using the relation between $\rho_{\rm mod}$ and $\mathbf{r}_N$. Note that $\partial \chi^2/\partial \mathbf{v}_{N-1/2}(\mathbf{q}) \equiv 0$ since particle velocities are not used in our definition of χ^2. The second is the Particle-Mesh transformation, which obtains $\partial \chi^2/\partial \mathbf{r}_n(\mathbf{q})$ and $\partial \chi^2/\partial \mathbf{v}_{n-1/2}(\mathbf{q})$ through the values of $\partial \chi^2/\partial \mathbf{r}_{n+1}(\mathbf{q})$ and $\partial \chi^2/\partial \mathbf{v}_{n+1/2}(\mathbf{q})$ obtained in a previous step, using the relations between $[\mathbf{r}_n(\mathbf{q}), \mathbf{v}_{n-1/2}(\mathbf{q})]$ and $[\mathbf{r}_{n+1}(\mathbf{q}), \mathbf{v}_{n+1/2}(\mathbf{q})]$ given by the PM model. Finally, the Zel'dovich transformation relates $[\mathbf{r}_{\rm i}(\mathbf{q}), \mathbf{v}_{\rm i}(\mathbf{q})] = [\mathbf{r}_0(\mathbf{q}), \mathbf{v}_0(\mathbf{q})]$ to $\delta_j(\mathbf{k})$. We introduce a transitional matrix,

$$\mathbf{\Psi}(\mathbf{q}) = N_{\rm c}^3 \left[\frac{\partial \chi^2}{\partial \mathbf{r}_{\rm i}(\mathbf{q})} + \frac{\partial \chi^2}{\partial \mathbf{v}_{\rm i}(\mathbf{q})} H_{\rm i} a_{\rm i}^2 f(\Omega_{\rm i}) \right] , \tag{30}$$

and derive the expression of the likelihood term of the Hamiltonian force for the real part of $\delta(\mathbf{k})$ as

$$F_{\rm re}(\mathbf{k}) = \frac{2D(a_{\rm i})}{k^2} \mathbf{k} \cdot \mathbf{\Psi}_{\rm im}(\mathbf{k}) \,, \tag{31}$$

and for the imaginary part as

$$F_{\rm im}(\mathbf{k}) = -\frac{2D(a_{\rm i})}{k^2} \mathbf{k} \cdot \mathbf{\Psi}_{\rm re}(\mathbf{k}) \,. \tag{32}$$

Here $\mathbf{\Psi}_{\rm re}(\mathbf{k})$ and $\mathbf{\Psi}_{\rm im}(\mathbf{k})$ are, respectively, the real and imaginary parts of $\mathbf{\Psi}(\mathbf{k})$, the Fourier transform of $\mathbf{\Psi}(\mathbf{q})$.

The details of the calculation of all the terms in the likelihood term of the Hamiltonian force are given in Appendix B.

3. N-body Simulations and the Performance of the PM model

3.1. N-body Simulations

In this paper, we use four N-body simulations to test the performance of our HMC+PM method. These simulations are obtained using Gadget-2 (Springel 2005). The initial conditions are set up using the method presented in Section 2.2.1. Two of them, which are referred to as L300A and L300B, assume a spatially flat ΛCDM model, with the present density parameter $\Omega_{\rm m,0} = 0.258$, the cosmological constant $\Omega_{\Lambda,0} = 0.742$ and the baryon density parameter $\Omega_{\rm b,0} = 0.044$, and with the power spectrum obtained using the linear transfer function of Eisenstein & Hu (1998) with an amplitude specified by $\sigma_8 = 0.80$. The CDM density field of each simulation was traced by 512^3 particles in a cubic box with a side length of 300 h^{-1}Mpc. The other two simulations, referred to as L100A and L100B, assume the same cosmological model as the L300 simulations, but use 512^3 particles to trace the evolution of the cosmic density field in a smaller, 100 h^{-1}Mpc box. The initial redshifts for the L300 and L100 simulations are set to be 36 and 72, respectively. For the cosmological model adopted here, the characteristic nonlinear scale at the present is about $7\,h^{-1}$Mpc, corresponding to a wave-number $k \simeq 0.15\,h$Mpc^{-1}.

3.2. Parameters and Performance of the PM Model

The accuracy and reliability of the HMC method relies on the adopted model of structure evolution. This is the main reason why we propose to employ the PM model, instead of other simpler models with lower accuracy, to evolve the cosmic density field. In principle, the PM model can yield a density field with high precision, as long as the grid cell size, $l_{\rm c} = L/N_{\rm c}$, and the time step, characterized by $\log(1+z_{\rm i})/N_{\rm PM}$, are chosen to be sufficiently small. In practice, however, it is feasible only to adopt a finite cell size and a finite time step, because of limited computational resource. It is thus necessary to explore the dependence of the quality of the PM model on $l_{\rm c}$ and $N_{\rm PM}$, which can then help us to properly set the parameters in our HMC. One way to quantify the quality of a structure evolution model is to measure its similarity to the density field obtained from a high-resolution simulation with the same initial condition. The similarity between any two density fields, X and Y, can be quantified by using the phase correlation of their Fourier transforms (see e.g. TZ12; Kitaura & Heß 2013),

$$C_p(k, X, Y) = \frac{\langle X(\mathbf{k})Y^*(\mathbf{k})\rangle_{\mathbf{k}}}{\sqrt{\langle|X(\mathbf{k})|^2\rangle_{\mathbf{k}}\langle|Y(\mathbf{k})|^2\rangle_{\mathbf{k}}}}\,. \tag{33}$$

Evidently, $C_p(k) = 1$ implies that the two fields have exactly the same phase, while $C_p(k) = 0$ indicates null correlation, for the Fourier mode in question.

As an example, we show in Figure 1 such phase correlation for a PM model using $l_{\rm c} = 1.5\,h^{-1}$Mpc. The upper right panel shows the phase correlations between the two L300 simulations and the corresponding PM density fields at redshift zero. The number of PM steps ($N_{\rm PM}$)

used here is 10. The two curves are almost identical, suggesting that the quality of the PM model is insensitive to sample variance. At large scales, the PM density fields almost perfectly match the original simulations. Even at the highly non-linear scale $k \sim 2.0\,h\mathrm{Mpc}^{-1}$, the correlation coefficient is still larger than 0.6. For comparison, the correlations for PM models using $N_{\rm PM} = 5$, 10 and 40 are shown in the upper left panel. Here results are presented only for L300A. As expected, the quality of the PM model improves with increasing $N_{\rm PM}$. The improvement is large at $N_{\rm PM} \leq 10$, but becomes saturated at $N_{\rm PM} > 10$. The reason is that once the typical motion of particles in one time step is much less than the grid cell size, as is the case for $N_{\rm PM} = 40$ and $l_{\rm c} = 1.5\,h^{-1}$Mpc, the use of a higher time resolution becomes unnecessary.

In order to further characterize the phase correlation, we introduce a quantity, k_{95}, which is defined to be the wavenumber at which the correlation coefficient defined in equation (33) decreases to 0.95. A larger k_{95} therefore indicates a more accurate model prediction. We show k_{95} as a function of $N_{\rm PM}$ for various $l_{\rm c}$ in the left panel of Figure 2. For all the cell sizes examined, k_{95} first increases with $N_{\rm PM}$, and then remains at an almost constant level. For a given grid cell size l_c, there is thus an upper limit in the performance of the PM model, consistent with the results shown in Figure 1. Of course, the level of the best performance increases as l_c decreases. For instance, the value of k_{95} for $l_{\rm c} = 3$, 1.5 and $0.75\,h^{-1}$Mpc are about 0.38, 0.80 and $1.78\,h\mathrm{Mpc}^{-1}$, respectively (see the upper right panel of Figure 2), roughly proportional to $1/l_{\rm c}$. Moreover, these results suggest that, for a given l_c, there is a minimum $N_{\rm PM}$ such that the performance of the PM model almost reaches its best and any further increase in $N_{\rm PM}$ no long makes significant improvement. This minimum $N_{\rm PM}$ roughly scales as $1/l_{\rm c}^2$, as shown in the lower right panel of Figure 2, and is about 3, 10 and 40 for $l_{\rm c} = 3$, 1.5 and $0.75\,h^{-1}$Mpc, respectively.

For given $N_{\rm PM}$ and $l_{\rm c}$, significant bias can exist in the PM density field relative to the real density field. In order to correct for this effect, following TZ12, we introduce a density transfer function, $T(k)$, which is obtained by cross-correlating the original simulation and the PM density field [equation (27)]. Note that introducing $T(k)$ into the calculation of the final density field does not change the phase correlation shown above. As an example, the lower left panel of Figure 1 shows the transfer function for $l_{\rm c} = 1.5\,h^{-1}$Mpc and $N_{\rm PM} = 5$ or 10. As expected, $T(k)$ is almost unity at large scales and increases gradually with increasing k until $k \sim 1.5\,h\mathrm{Mpc}^{-1}$. An downturn is observed in the transfer functions at small scales, indicating a rapid decline in the correlation between the two density fields at such scales. Since the PM model with $N_{\rm PM} = 10$ (referred to as PM10) is more accurate than PM5, the transfer function for the PM10 model is closer to unity than that for the PM5 model. Similar to the phase correlations, the transfer functions are insensitive to sample variance (see the lower right panel of Figure 1). In what follows, PM model really means PM model combined with the corresponding transfer function.

The other way to reduce the bias produced by the inaccuracy of the PM model at small scales is to smooth both the PM density field and the input density field at small scales before using them to calculate the likelihood function in the HMC. Here we investigate which smoothing scale, $R_{\rm s}$, is suitable for our purpose. To this end, we calculate the two point correlation functions for

both the PM density field ($\xi_{\rm PM}$) and the original, simulated density field ($\xi_{\rm SIM}$), both smoothed with the same smoothing scale. Figure 3 shows the ratio, $\xi_{\rm PM}/\xi_{\rm SIM}$, for a number of smoothing scales. The results are shown for three PM models, one with $l_{\rm c} = 1.5\,h^{-1}$Mpc and $N_{\rm PM} = 10$, another with $l_{\rm c} = 1\,h^{-1}$Mpc and $N_{\rm PM} = 20$, and the third with $l_{\rm c} = 0.75\,h^{-1}$Mpc and $N_{\rm PM} = 40$ (hereafter referred to as PM40). We note again that all the density fields are corrected with the density transfer functions. The model predictions are in good agreement with the original ones at large scales for all models, independent of the smoothing scale adopted. At small scales, however, the PM density fields are less clustered than the simulated ones. This discrepancy is significant only when the smoothing scale, in units of $l_{\rm c}$, is chosen to be too small, but almost vanishes for $R_{\rm s} \geq 2l_{\rm c}$. This basically says that PM density field is inaccurate on scales below a couple of grid cells and the difference between the model prediction and the input field on such scales should be suppressed with smoothing. However, choosing a too large $R_{\rm s}$ will cause loss of information on small scales. As a compromise we will use $R_{\rm s} = 3l_{\rm c}$ as our fiducial value.

4. Applications and Tests of the HMC+PM Method

4.1. Setting Parameters for the HMC

Before describing the applications of our PM based HMC (HMC+PM), we briefly describe how to specify the parameters in the HMC and in the PM model. We divide the simulation boxes into $N_{\rm c}^3$ grid cells and use a Gaussian kernel with a smoothing scale of $R_{\rm s}$ to smooth the particle distributions at redshift zero on to the grids. The resultant density fields, denoted by $\rho_{\rm si}(z = 0)$, are what we want to match in the reconstructions [i.e. $\rho_{\rm inp} = \rho_{\rm si}(z = 0)$].

Our dynamic model consists of two parts. First, the Zel'dovich approximation has one parameter, the initial redshift $z_{\rm i}$. In the present paper we set $z_{\rm i} = 36$, the same as that for the initial conditions of the L300 simulations. Second, the PM model (including the transfer function) has two parameters, the grid cell size, $l_{\rm c}$, and the number of time steps, $N_{\rm PM}$. The computation time for a PM model is proportional to $N_{\rm PM}$ and $1/l_{\rm c}^3$. As a compromise between computation time and model precision, we adopt two PM models, PM10 with $l_{\rm c} = 1.5\,h^{-1}$Mpc and $N_{\rm PM} = 10$, which is implemented in the reconstructions of the L300 series; PM40 with $l_{\rm c} = 0.75\,h^{-1}$Mpc and $N_{\rm PM} = 40$, used in the reconstructions of the L100 series. The corresponding $N_{\rm c}$ is 200 for L300 and 134 for L100.

According to the tests shown above, we choose the smoothing scale $R_{\rm s} = 3l_{\rm c}$ in our HMC runs to make sure that the bias in the PM density field on small scales is sufficiently suppressed. A series of tests were done in W13 to tune other HMC parameters. Following their results, we adopt $n_{\rm max} = 13$, $\tau_{\rm max} \approx 0.1$ and set $\sigma_{\rm inp}(\mathbf{x}) = \mu\rho_{\rm si}(\mathbf{x})$ with $\mu = 0.5$. The weight field $w(\mathbf{x})$ is set to be unity for all grid cells.

4.2. Applications to Simulated Density Fields

We use the four N-body simulations, L300A, L300B, L100A and L100B, to test our HMC+PM method. Note again that PM10 and PM40 are adopted for the reconstructions of the L300 and L100 series, respectively. The input density field $\rho_{\rm inp} = \rho_{\rm si}(z = 0)$ is smoothed with a smoothing scale $R_{\rm s} = n_{\rm s} l_{\rm c}$, and $n_{\rm s}$ are set to be 3 and 4 for L300 and L100, respectively. The initial set of $\delta(\mathbf{k})$ is randomly drawn from the prior Gaussian distribution, $G(\delta(\mathbf{k}))$, as shown in equation (1). The Hamiltonian masses are computed twice during the entire process. The first time is at the beginning. After proceeding 50 or 80 accepted chain steps, the mass variables are updated once with the current Hamiltonian forces and retained all the way to the end. Computations are made for 2000 (3000) HMC steps for the L300 (L100) series, and the acceptance rates for the reconstructions of the L300 and L100 series are about 83% and 96%, respectively. The left and middle panels of Figure 4 show $\chi^2_w \equiv \chi^2 / \sum_{\mathbf{x}} w(\mathbf{x})$ as a function of the chain step. The value of χ^2_w drops sharply at the beginning (the burn-in phase), and then remains almost constant after about 500 - 1000 chain steps (the convergence phase). The χ^2_w values of the converged steps are about 0.004 (L300) and 0.002 (L100), showing that the predicted density fields after convergence match the input ones well.

For the reconstruction of the L100 series, further HMC process is carried out to increase the reconstruction accuracy. This time the input density field is still $\rho_{\rm si}$ but smoothed with a smaller smoothing scale, $R_{\rm s} = 3 l_{\rm c} = 2.25\, h^{-1}$Mpc. The initial set of $\delta(\mathbf{k})$ is not randomly generated, but taken from the linear density field output at the 2700th step of the first HMC process, and so are the Hamiltonian masses. The new fictitious systems are then evolved for additional 2000 steps, and the acceptance rates here are about 95%. The right panel of Figure 4 shows χ^2_w as a function of chain step for the additional runs. At the first step, χ^2_w is about 0.02, much larger than the final one of the first HMC run. It is ascribed to the smaller smoothing scale adopted here. One can see that two-phase behavior is conspicuous too. After a quick decline within the first 200 steps, χ^2_w converges to about 0.004. Since the initial set of $\delta(\mathbf{k})$ is not random, the decreasing in the amplitude of χ^2_w in the second part of the HMC is much slower. We note that the two-phase behavior is commonly seen in HMC runs (e.g. Hanson 2001; Taylor, Ashdown, & Hobson 2008). As discussed in W13, the fictitious system in question actually mimics a cooling system in a gravitational potential well. The reset of momenta at the beginning of every chain step (see Section 2.1) is an analog to the 'cooling' process, which makes the system fall continuously and eventually reach the bottom region of the potential well (i.e. around the posterior peak we are searching for).

On the scale of $4.5\, h^{-1}$Mpc ($2.25\, h^{-1}$Mpc), the *RMS* (root mean square) difference between $\rho_{\rm inp}$ and $\rho_{\rm mod}$ is about $\mu\sqrt{2\chi^2_w} \simeq 4.5\%$ (4.6%) for the L300 (L100) series. This is an accurate match, indicating that the second constraint in our reconstruction, namely that $\rho_{\rm mod}$ matches $\rho_{\rm inp}$, is well satisfied. In order to check whether our reconstruction also meets the first constraint, i.e., the prior Gaussian distribution with a given linear power spectrum, we show in Figure 5 the power spectra measured from the reconstructed linear density fields at the final chain steps, with the original linear spectra overplotted for comparison. Over the entire range of wavenumbers, the

reconstructed initial spectra are in good agreement with the original ones. Examining closely, however, we see some small deviations. For example, the reconstructed linear spectra contain a small bump (less than 10%) at the intermediate scale ($k \sim 0.9\,h\mathrm{Mpc}^{-1}$ in the L100 series). Similar but significantly stronger bump is also seen in the reconstructed linear spectra of W13, Kitaura (2013, their figure 2) and Ata, Kitaura, Müller (2014).

In order to understand the origin of this discrepancy, we apply our HMC+PM reconstruction with PM density fields as input. Since the input field is generated with the same PM model as that used in the HMC, no bias is expected from the inaccuracy of the PM model. As shown in Appendix C, even in such cases, there is still deviation on scales $\sim R_s$, below which the prior term of the Hamiltonian force starts to dominate over the likelihood term. Fortunately, the deviation is quite small (typically less than 10%) and can be moved to small scales of no practical importance by adopting a sufficiently small l_c (so that R_s is sufficiently small).

For a random Gaussian field, $d_{\mathrm{n},j}(\mathbf{k}) \equiv \delta_j(\mathbf{k})/\sqrt{P_\mathrm{lin}(k)/2}$ should obey a Gaussian distribution with $\sigma = 1$, independent of the wavenumber k. Figure 6 shows the distributions of $d_{\mathrm{n},j}(\mathbf{k})$ for three different wave-numbers, together with a Gaussian function with $\sigma = 1$. These distributions match the Gaussian distribution very well even in the large $|d_{\mathrm{n},j}(\mathbf{k})|$ tails. The fluctuations at the tails are due to small number statistics. We have also calculated the third- and fourth-order moments of the distributions and estimated the corresponding skewness and kurtosis (using equations 6.43 and 6.44 in Mo, van den Bosch, & White 2010). Both are found to be very close to zero. All these demonstrate that our reconstruction recovers the Gaussianity of the linear density field very well.

At small scales, the Hamiltonian forces are dominated by the prior term, as the likelihood term is strongly suppressed by the smoothing (see Appendix C). Consequently the phases of the reconstructed $\delta(\mathbf{k})$ are expected to be random on small scales. To quantify on which scales the reconstructed $\delta(\mathbf{k})$ matches the original ones well, we measure the phase correlation between the two linear density fields. The results are shown as solid lines in the two left panels of Figure 7. For the L300 series, the correlation coefficients are larger than 0.95 at $k < 0.28\,h\mathrm{Mpc}^{-1}$, and decline gradually to 0.5 at $k \sim 0.47\,h\mathrm{Mpc}^{-1}$. For the L100 series the phase correlation is even better, with the correlation coefficient reaching 0.95 at $k \sim 0.36\,h\mathrm{Mpc}^{-1}$ and declining to 0.5 at $k \sim 0.85$. The correlation is still significant ($C_p \sim 0.1$) at $k \sim 1.3\,h\mathrm{Mpc}^{-1}$. The improvement is clearly due to the better PM model that can recover better the phase information on small scales. Note that the results of the two reconstructions in the same series are very similar, demonstrating again the robustness of our HMC+PM method.

So far we have shown the results of the linear density field obtained from the final chain step of each reconstruction. We have also checked the results at other steps after burn-in and found that they have almost the same statistical properties as the final chain step. Because our goal here is to reconstruct $\delta(\mathbf{k})$ rather than to draw a posterior ensemble of linear density fields, we will not present the results for chain steps other than the final one.

5. N-body simulations of the reconstructed initial density fields

To further investigate the accuracy of our method, we use the reconstructed linear density fields to set up initial conditions, and evolve them to the present day with the N-body code Gadget-2 (Springel 2005). These new simulations are referred to as constrained simulations (CS). The initial conditions are sampled with the same number of N-body particles as in the corresponding original simulations. The Nyquist frequency for these initial conditions is larger than $k_{\rm rc} = N_{\rm c}\pi/L$, the largest working frequency of our HMC method. We complement the Fourier modes at $k > k_{\rm rc}$ by sampling $\delta(\mathbf{k})$ from the prior Gaussian distribution, $G(\delta(\mathbf{k}))$. In the following a suffix '-CS' is added after the name of an original simulation to denote the corresponding CS. For example, L100A-CS denotes the CS of L100A. The corresponding density field of a CS is denoted by $\rho_{\rm cs}$.

The CS power spectra at redshift zero are presented in Figure 5. As can be expected from the good accuracy in the reconstructed linear density fields, the CS power spectra match their original counterparts well. The phase correlations between $\rho_{\rm cs}$ and $\rho_{\rm si}$ at $z = 0$ are shown as dashed lines in the left two panels of Figure 7. The correlations are very tight. For example, the L100-CSs almost perfectly match the original ones all the way to non-linear scales, $k \sim 1.0\,h{\rm Mpc}^{-1}$. Even at highly non-linear scales ($k \sim 3.4\,h{\rm Mpc}^{-1}$), about half of the phase information is recovered. The correlations are much stronger than that obtained from the HMC+MZA method. The latter predicts a more rapid decrease of the correlation function with increasing k, reaching 0.5 at $k \sim 1\,h{\rm Mpc}^{-1}$ (W13). The improvement of our HMC+PM over the HMC+MZA is clearly due the more accurate PM model used in the HMC+PM for evolving the cosmic density field. The phase correlation between $\rho_{\rm cs}$ and $\rho_{\rm si}$ is also much tighter than that of the corresponding linear density fields (solid lines). For instance, at $k = 1\,h{\rm Mpc}^{-1}$ the correlation between linear density fields is only modest for the L100 series, in contrast to the almost perfect correlation between the fully evolved density fields (dashed lines). This phenomenon can be readily interpreted by non-linear mode coupling, in which the small-scale power of a non-linear density field is partly produced by the large scale power (e.g. Tassev & Zaldarriaga 2012a). Thus, even phase correlation is absent on small scales between the reconstructed and original linear fields, it can be generated by the phase correlation on large scales that is present in the linear fields.

Since non-linear effect is more important at lower redshift, the mode coupling effect is expected to be less significant at high z. To demonstrate this, we show the phase correlations between $\rho_{\rm cs}$ and $\rho_{\rm si}$ at five different redshifts, together with that for the initial density fields, in the right panels of Figure 7. Take the results for L300A as an example (the upper right panel). The correlation at $z = 4$ is very similar to that of the linear field, indicating that mode coupling has not taken its effect. At $z = 2$, the correlation coefficient is enhanced significantly at $k \sim 0.9\,h{\rm Mpc}^{-1}$, but remains unchanged at $k \sim 0.5\,h{\rm Mpc}^{-1}$. As the evolution proceeds to $z = 0.5$, the effect becomes visible over the entire range of wave-numbers, where the initial phases are not well constrained. Similar behavior is also found for L100A, as shown in the lower right panel. This demonstrates again that an accurate dynamic model of structure evolution is required in order to have accurate reconstruction in the non-linear regime.

In Figures 8 and 9, we compare mass densities in the CSs with those in the input simulations at four different redshifts. The density fields are smoothed within Gaussian windows with radii the same as $R_{\rm s}$ adopted in the corresponding HMC runs (i.e. $4.5\,h^{-1}$Mpc for L300, and $2.25\,h^{-1}$Mpc for L100). The three contours in each panel encompass 67%, 95% and 99% of the grid cells in the whole simulation box. The densities of the CS in individual cells are tightly and linearly correlated with the original ones over a large dynamic range; for L100 this correlation extends from $\rho/\bar{\rho} = 0.1$ to about 50 at redshift zero. The constrained simulations do not show any significant bias, and at $z = 0$ the typical dispersion in the $\rho_{\rm si}$ - $\rho_{\rm cs}$ relation is about 0.05 dex for both L300 and L100. Interestingly, the typical dispersion does not depend significantly on redshift; the seemingly looser relations at higher z are due to the smaller ranges in density. However, at high z the dispersion is larger for higher densities. The reason for this is that small-scale modes are not well constrained in the initial conditions and mode coupling has not fully developed at high z.

Figure 10 shows some renderings of the three-dimensional density fields of both L100A (left) and L100A-CS (right) at four different redshifts. Particles are color-coded by local densities calculated using the Delaunay density estimator developed by Schaap & van de Weygaert (2000), with white clumps corresponding to massive halos. The two maps look very similar at $z = 0$. Almost all large structures in the original simulation, such as massive clusters, filaments, and underdense voids, and even some small details, are well reproduced. In particular, the CS accurately recovers the topological structures of the cosmic web, suggesting that the large scale environment of dark matter halos, which is an important factor affecting halo formation (see e.g. Wang et al. 2011), is well reproduced. At higher z, the similarity is also remarkable, in particular on large scales. On small scales, there are noticeable differences which become more significant with increasing redshift, consistent with the phase correlation results shown in Figure 7. These comparisons demonstrate that our method can recover the formation history of the large-scale structure with high accuracy.

Halos are the key components in the build-up of structure in current CDM cosmogony and are thought to be the hosts of galaxies. Therefore, a proper reconstruction of halo properties is essential for our future study of galaxies and their relation with the large-scale environment. In a forthcoming paper, we will compare in detail the internal properties, environment and assembly histories of halos and other structures between the input simulations and CSs. Here we only focus on the halo mass function $n(M_{\rm h}) = {\rm d}n/{\rm d}\log M_{\rm h}$. We identify halos using the standard friends-of-friends (FOF) algorithm (Davis et al. 1985) with a link length that is 0.2 times the mean inter-particle separation. Following Warren et al. (2006), we calculate the mass of a halo as $M_{\rm h} = m_{\rm p}N_{\rm h}(1 - N_{\rm h}^{-0.6})$, where $m_{\rm p}$ is the particle mass and $N_{\rm h}$ is the total particle number in a halo. This mass definition is used to correct for some statistical effects of using only finite number of particles to estimate the mass of a FOF halo.

The halo mass functions at various redshifts obtained from L300A-CS and L100A-CS are shown in Figures 11 and 12, with the error-bars representing Poisson fluctuations in individual mass bins. These CS mass functions are well matched by both the theoretical prediction (Sheth, Mo, & Tormen 2001) and the ones obtained from the corresponding original simulations. To inspect the results in

more detail, we show in Figure 13 the ratio of halo mass function between the CS and the original simulation, $n_{\rm cs}(M_{\rm h})/n_{\rm si}(M_{\rm h})$. If $n_{\rm si}(M_{\rm h}) = 0$ in a mass bin, it is replaced by the corresponding value of the theoretical halo mass function. In order to reduce the fluctuations at the high mass end, halos are re-binned into fewer mass bins. As one can see, although the halo mass functions of the reconstructed density fields are in overall good agreement with the original ones, there is very weak, but noticeable bias. Such bias is not expected, as the initial density field is well reproduced in both power spectrum and Gaussianity. As we will see below, the reconstruction apparently can introduce some very subtle non-Gaussian effect, which in turn can affect the precision of the predicted halo mass function. This effect becomes more important when a less accurate model of structure evolution is adopted.

6. Comparing results obtained from different models of structure evolution

A number of different structure evolution models have been adopted in the literature for the reconstruction of the initial cosmic density field. Here we compare the performances of some of them, showing that our HMC+PM is superior.

In our early paper (W13), we adopted the MZA model, developed by TZ12. The phase correlation between the density field reconstructed from the HMC+MAZ method with the input density field is plotted in the upper left panel of Figure 1. For this model $k_{95} \sim 0.33\,h{\rm Mpc}^{-1}$, very similar to that shown in TZ12 for different cosmological parameters. The phase correlation for 2LPT, which is adopted by Jasche & Wandelt (2013) and Kitaura (2013) to reconstruct the initial density fields from the galaxy density field, has $k_{95} = 0.37\,h{\rm Mpc}^{-1}$, as shown in TZ12. More recently, Heß, Kitaura, & Gottlöber (2013) employed a modification of the 2LPT, the ALPT developed by Kitaura & Heß (2013), in their reconstruction. As shown in figure 4 of Kitaura & Heß (2013), the ALPT model can achieve $k_{95} \sim 0.45\,h{\rm Mpc}^{-1}$, better than the 2LPT. For our HMC+PM method, Figure 2 shows that the value of k_{95} that is achieved by PM5 and PM10 are 0.67 and $0.80\,h{\rm Mpc}^{-1}$, respectively, much better than all these earlier models. Indeed, our test showed that the performances of the 2LPT and the ALPT are only between our PM models with $N_{\rm PM} = 2$ and 3. Clearly, the PM model with a modest number of time steps is by far the best model that can be implemented into the HMC method.

To make further tests, linear density field is reconstructed from the L300A simulation using both the HMC+MZA and the HMC+PM5. The density transfer function for PM5 is given in the lower left panel of Figure 1, while that for MZA is adopted from TZ12. Since the HMC runs employing the same model of structure evolution give very similar results (see e.g. Figure 7), only one run is performed for each model. Similar to the finding in W13, the reconstructed linear power spectra from these two runs match well the original ones, except a significant bump on intermediate scales. We follow W13 to 'renormalize' the amplitudes of the modes in the bump so that the power spectrum matches the original one. As shown in W13, even with the renormalization the distributions of $d_{{\rm n},j}(\mathbf{k}) = \delta_j(\mathbf{k})/\sqrt{P_{\rm lin}(k)/2}$ are still very close to Gaussian with $\sigma = 1$. We use

the linear density fields so obtained to set up initial conditions, and follow the evolutions of the density fields with the N-body code described above.

Figure 14 shows the mass function ratio, $n_{\rm cs}(M_{\rm h})/n_{\rm si}(M_{\rm h})$, at $z = 0$ for the three models, HMC+PM10, HMC+PM5, and HMC+MZA. The halo mass function for the MZA model deviates significantly from the original one; it produces too many massive halos at $M_{\rm h} > 10^{14.3}\,h^{-1}{\rm M}_{\odot}$ and too few halos of $10^{13.5}\,h^{-1}{\rm M}_{\odot}$. Second, there is a clear trend that the mass function in the CS gradually converges to the original one as the accuracy of the model increases, in the order from MZA to PM5 to PM10. For PM10 the CS mass function is already quite close to the original one. Recently, Heß, Kitaura, & Gottlöber (2013) found that their CSs of the linear density fields constructed from the ALPT model significantly overproduce massive halos and underproduce small-mass halos relative to the reference mass functions. This is exactly the same as we find here when a model of low accuracy is used to evolve the cosmic density field, although the Bayesian approach they adopted is different from ours. The deviation they found is therefore more likely a result of the inaccuracy of the ALPT, rather than due to the cosmic variance.

One possible reason for this deviation is that the HMC induces spurious correlations in the reconstructed $\delta(\mathbf{k})$ if the model of structure evolution is not sufficiently accurate. Most of the approximations, which cannot properly handle highly non-linear dynamics on small scales, tend to underestimate the density in high density regions, in particular around halos. Thus the parameter χ^2, which the HMC process attempts to minimize, is contributed by two different sources. One is the difference between the reconstructed and the real $\delta(\mathbf{k})$, and the other is the underestimation of the power spectra on small scales due to the use of approximate dynamics. During the evolution of the Hamiltonian system, the HMC tries to tune $\delta(\mathbf{k})$ to compensate for the lost power in two ways. One is to enhance the amplitude of $\delta(\mathbf{k})$, which is seen in the reconstructed linear power spectra (see W13; Kitaura 2013; Ata, Kitaura, Müller 2014). The other is to introduce some non-Gaussianity into $\delta(\mathbf{k})$.

To verify the latter probability, we first derive a smoothed version of the reconstructed linear density field, $\delta(\mathbf{x}, r_{\rm th})$, where the smoothing is done with a top-hat kernel with radius $r_{\rm th}$. We then measure the variance ($\kappa_2 \equiv \sigma^2$), skewness (κ_3) and kurtosis (κ_4) of the smoothed field. For a random Gaussian field, it is easy to prove that $\kappa_l = 0$ for all $l > 2$. Thus any non-zero high-order κ_l signifies non-Gaussianity. Figure 15 shows the three quantities as functions of $r_{\rm th}$ for the original linear density field and for the reconstructed linear density fields based on PM10, PM5 and MZA. For comparison, we also present the results measured from 19 random Gaussian fields.

The three reconstructions exhibit almost identical $\sigma^2(r_{\rm th})$ as the original one, which is expected since $\sigma^2(r_{\rm th})$ is directly related to the linear power spectrum. However there are clear differences in κ_3 and κ_4 between the three reconstructions and the original linear density field. By construction, these two quantities should be close to zero. The reconstructed linear density field based on PM10 exhibits small nonzero κ_3 on small scales, but the deviation is still within the grey region which represents the variance among the 19 random Gaussian fields. The situation is very similar for

κ_4. Thus, no significant signal for non-Gaussianity is present in the reconstructed $\delta(\mathbf{k})$ based on PM10. In contrast, the non-Gaussianity is quite significant for PM5 and is the strongest for MZA. Such non-Gaussianity is hard to see in the distribution function of $\delta(\mathbf{k})$ but is the source of bias in the predicted halo mass function. As the densest and massive objects in the cosmic density field, massive halos are sensitive to the tail of the density distribution. These tests support our hypothesis that the origin of the deviation in halo mass function is non-Gaussianity.

Another potential issue is the smoothing scale $R_{\rm s}$ adopted for the three tests shown here, all being $3l_{\rm c} = 4.5\,h^{-1}$Mpc. According to our results of the two-point correlation function analysis (Section 3.2), this smoothing scale can effectively erase the difference between the model prediction of PM10 and the simulation, and so the result of the halo mass function is not biased by the inaccuracy of the model. For PM5 and MZA, however, $R_{\rm s} = 4.5\,h^{-1}$Mpc may be too small to get rid of the difference between the model and the simulation. This again shows that, in order to decrease the smoothing scale $R_{\rm s}$, so as to increase the accuracy of the reconstruction, and simultaneously to maintain Gaussianity, a highly accurate model of structure evolution is required. For example, the HMC+PM40 model with $R_{\rm s} = 2.25\,h^{-1}$Mpc predict a phase correlation that is significantly tighter than the prediction of the HMC+PM10 model. Consequently the halo mass function obtained is also in better agreement with the original one.

7. Summary and Discussion

Following the spirit of our previous paper (W13, see also Jasche & Wandelt 2013), we have developed a HMC method to reconstruct the linear (initial) density field from a given input non-linear density field at low redshift. This method allows us to generate the linear density field based on a posterior probability distribution function including both a prior term and a likelihood term. The prior term ensures that the reconstructed linear density field obeys a Gaussian distribution with a given power spectrum. The likelihood is designed to ensure that the evolved density field from the reconstructed linear density field matches the input non-linear density field. To improve the accuracy of the reconstruction, we have combined the HMC with the PM dynamics. The Hamiltonian force is the most important quantity that guides the chain steps, and we have worked out how to compute the Hamiltonian force for the PM model.

To optimize the parameters in the PM model, we have made a series of tests to investigate how the quality of the PM model predictions depend on the grid cell size, $l_{\rm c}$, and the number of time steps, $N_{\rm PM}$. The minimum $N_{\rm PM}$ required for the PM model to approach its best quality roughly scales as $1/l_{\rm c}^2$, and the wavenumber below which the PM model is reliable scales as $1/l_{\rm c}$. As a compromise between the accuracy of model prediction and computation time, we have made HMC runs with two choices, one with $l_{\rm c} = 1.5\,h^{-1}$Mpc, and the corresponding minimum number of timesteps is $N_{\rm PM} = 10$; the other one has $l_{\rm c} = 0.75\,h^{-1}$Mpc and the minimum number of time steps is $N_{\rm PM} = 40$. To increase the accuracy of model prediction, a density transfer function, which is very easy to obtain, is used. The PM10 model can produce more than 95% of the phase

information in the corresponding high-resolution N-body simulation down to a scale corresponding to $k = 0.8\,h\mathrm{Mpc}^{-1}$. The PM40 model is much more accurate, recovering more than 95% of the phase information all the way down to a highly non-linear scale, $k = 1.78\,h\mathrm{Mpc}^{-1}$. The discrepancy between the PM prediction and the input field on small scales need to be suppressed in a HMC run. Based on our two-point correlation function analysis, this can be done with a Gaussian filter with a radius $R_\mathrm{s} \approx 3l_\mathrm{c}$.

We have used four high-resolution N-body simulations as inputs to test the performance of our HMC+PM method. The Fourier modes of the reconstructed linear density fields obey well a Gaussian distribution with variance that is well matched by the original linear power spectrum.The phase-correlation coefficient between the reconstructed and original linear density fields is close to unity on large scales and declines gradually to 0.5 at $k \sim 0.85\,h\mathrm{Mpc}^{-1}$ and $k \sim 0.47\,h\mathrm{Mpc}^{-1}$ for the HMC+PM40 and HMC+PM10 runs, respectively. The *RMS* in the difference between the original (input) and modeled density fields are only about 4.6%. A weak discrepancy appears around the scale where the ratio between the likelihood and prior terms of the Hamiltonian force is about one, and is due to the compromise the HMC makes between these two terms.

As additional tests, we have compared the original simulations with the corresponding constrained simulations (CS) that are evolved from the reconstructed linear density fields with a high-resolution N-body code. The density fields in the CS are found to match the original ones over a large dynamic range at various redshifts. The typical dispersions in the density-density relation are about 0.05 dex on the scale of $3l_\mathrm{c}$, almost independent of redshift. Visual inspection of the particle distributions also shows that the CSs can well reproduce the large scale structures and their evolution histories. For the HMC+PM40 (HMC+PM10) run, the phase correlation between the CS and the original simulation is very close to unity down to a scale corresponding to $k = 1.1\,h\mathrm{Mpc}^{-1}$ ($0.5\,h\mathrm{Mpc}^{-1}$), and remains larger than 0.5 all the way to the highly non-linear regime $k \sim 3.4\,h\mathrm{Mpc}^{-1}$ ($1.1\,h\mathrm{Mpc}^{-1}$). In addition the halo mass functions derived from the CSs match well those derived from the original simulations. The tests based on the four different simulations give very similar results, demonstrating the robustness of our method.

We have also investigated how the performance of the HMC method depends on the accuracy of the dynamical model of structure evolution adopted. For a given R_s, a low-quality dynamical model results in a large deviation in the halo mass function, and produces significant non-Gaussianity in the reconstructed linear density field. All these results demonstrate the importance of adopting accurate dynamics in the HMC approach of reconstruction, and our HMC+PM method provides such a scheme. The method can achieve very high accuracy as long as the available computational resource allows the implementation of a PM model with sufficiently small l_c and sufficiently large N_PM.

In the future, we will apply our HMC+PM method to generate the initial conditions for the structure formation in the local Universe using observational data. Since our method needs an input density field, the method developed by Wang et al. (2009) will be adopted to reconstruct

the present-day density field from the SDSS DR7 galaxy group catalog constructed by Yang et al. (2007). This halo-based reconstruction method has been tested in great detail in Wang et al. (2009; 2012; 2013) and has been applied to SDSS DR4 by Muñoz-Cuartas, Müller, & Forero-Romero (2011) and to SDSS DR7 by W13. Our HMC+PM method can also be applied to the $z \sim 2$ density field reconstructed from the Lyα forest data (Pichon et al. 2001; Caucci et al. 2008). The test based on mock spectra by Lee et al. (2014) suggested that the spatial resolution in such reconstruction can reach to a scale of $\sim 2\,h^{-1}$Mpc (in comoving units) at $z \sim 2$, which can be handled very easily with our method. These studies showed that there are significant uncertainties in the reconstructed density fields at a given redshift, which may eventually be the main source of uncertainties in future applications. We will come back to this in a forthcoming paper.

The reconstructed initial conditions can be used to run CSs with both dark matter and gas components. This offers a unique opportunity to investigate the formation and evolution of the galaxy population we directly observe. For example, we can model galaxy formation using halos extracted from the CSs combined with semi-analytical models of galaxy formation, or carry out gas simulations directly from the reconstructed linear density field. The comparison between the modeled galaxy population and the observed one is then conditioned on the same large-scale environments, and so the effect of cosmic variance is eliminated or reduced. Furthermore, the predicted distribution and state of the gas component can also be compared directly with observations of the Sunyaev-Zel'dovich effect, X-ray emission, and quasar absorption line systems, to provide a more complete picture about the interaction between dark matter, gas and galaxies.

Acknowledgments

We thank Yu Yu for useful suggestion and Kun Cheng for rendering the figures. This work is supported by the Strategic Priority Research Program "The Emergence of Cosmological Structures" of the Chinese Academy of Sciences, Grant No. XDB09010400, NSFC (11073017, 11233005, 11320101002, 11121062, 11033006, U1331201), NCET-11-0879. HJM would like to acknowledge the support of NSF AST-1109354 and the CAS/SAFEA International Partnership Program for Creative Research Teams (KJCX2-YW-T23).

A. Abbreviations, Terms and Quantities

- PM model: Particle-Mesh model;
- $l_{\rm c}$: the mesh cell size in a PM model;
- $N_{\rm PM}$: number of time-steps in a PM model;
- PM$N_{\rm PM}$: a PM model with $N_{\rm PM}$ time-steps;

- PM$N_{\rm PM}$ density field: the density field predicted by the corresponding PM model;
- Modeled density field: the density field predicted by a dynamical model of structure evolution;
- MZA: modified Zel'dovich approximation;
- HMC: Hamiltonian Markov Chain Monte Carlo;
- HMC+PM$N_{\rm PM}$: a HMC run using a specific PM model;
- HMC+MZA: a HMC run using MZA;
- Input density field or $\rho_{\rm inp}$: the density field used to constrain a reconstruction;
- Original quantities: quantities measured from or related to an input simulation;
- $R_{\rm s}$: the radius of the Gaussian kernel used to smooth both the input density field and the modeled density fields in a HMC run;
- Reconstructed linear density field: the linear density field reconstructed from an input density field;
- Reconstructed linear power spectrum: the linear power spectrum measured from a reconstructed linear density field;
- CS: constrained simulation, the simulation of a reconstructed linear density field;
- CS quantities: quantities measured from a CS.

We test HMC with three PM models: PM5, PM10 and PM40. The mesh cell size ($l_{\rm c}$) for PM5 and PM10 is $1.5\,h^{-1}$Mpc, and is $0.75\,h^{-1}$Mpc for PM40.

B. Calculations of the likelihood term of Hamiltonian force

Here, we provide the details of the Hamiltonian force calculation described in Section 2.3. For conciseness, we use N to replace $N_{\rm PM}$ in this appendix.

B.1. The χ^2 transformation

Following equation (13) in W13, we have

$$\frac{\partial\chi^2}{\partial\mathbf{r}_N(\mathbf{q})} = N_{\rm c}^3 \sum_{\mathbf{k}} \rho_{\rm d}^*(\mathbf{k}) \frac{\partial\rho_{\rm mod}(\mathbf{k})}{\partial\mathbf{r}_N(\mathbf{q})}\,, \tag{B1}$$

where $\rho_{\rm d}(\mathbf{x}) = [\rho_{\rm mod}(\mathbf{x}) - \rho_{\rm inp}(\mathbf{x})]\omega(\mathbf{x})/\sigma^2_{\rm inp}(\mathbf{x})$. Inserting the expression of $\rho_{\rm mod}$ given by equation (28) into the above expression, we have

$$\begin{aligned}\frac{\partial\chi^2}{\partial\mathbf{r}_N(\mathbf{q})} &= \sum_{\mathbf{x}}\frac{\partial\rho_{N,{\rm c}}(\mathbf{x})}{\partial\mathbf{r}_N(\mathbf{q})}\sum_{\mathbf{k}}\rho^*_{\rm d}(\mathbf{k})\frac{w_{\rm g}(R_{\rm s}k)T(k)}{w_{\rm c}(\mathbf{k})}{\rm e}^{i\mathbf{k}\cdot(\mathbf{L}-\mathbf{x})} \\ &= \sum_{\mathbf{x}}\sum_{\mathbf{q}_1}\frac{\partial w_{\rm c}(\mathbf{x}-\mathbf{r}_N(\mathbf{q}_1))}{\partial\mathbf{r}_N(\mathbf{q})}\rho_{\rm ds}(\mathbf{L}-\mathbf{x}) = \sum_{\mathbf{x}}\frac{\partial w_{\rm c}(\mathbf{x}-\mathbf{r}_N(\mathbf{q}))}{\partial\mathbf{r}_N(\mathbf{q})}\rho_{\rm ds}(\mathbf{L}-\mathbf{x})\,, \qquad \text{(B2)}\end{aligned}$$

where $\rho_{\rm ds}(\mathbf{x})$ is the Fourier transformation of $\rho^*_{\rm d}(\mathbf{k})w_{\rm g}(R_{\rm s}k)T(k)/w_{\rm c}(\mathbf{k})$ and $\mathbf{L} = (L, L, L)$ so ${\rm e}^{i\mathbf{k}\cdot\mathbf{L}} \equiv 1$. Note that $\partial w_{\rm c}(\mathbf{x} - \mathbf{r}_N(\mathbf{q}_1))/\partial\mathbf{r}_N(\mathbf{q})$ is nonzero only when $\mathbf{q}_1 = \mathbf{q}$. Moreover, $\partial w_{\rm c}(\mathbf{x} - \mathbf{r}_N(\mathbf{q}))/\partial\mathbf{r}_N(\mathbf{q})$ is nonzero only in a number of grid cells close to $\mathbf{r}_N(\mathbf{q})$, which can also be used to speed up the calculation of equation (B2). Note that χ^2 is independent of the final velocity field so that $\partial\chi^2/\partial\mathbf{v}_{N-1/2}(\mathbf{q}) = 0$.

B.2. The Particle-Mesh transformation

Starting from the last step $n = N$ where the derivatives of χ are obtained, we can obtain the derivatives successively at other steps. Suppose we have already obtained $\partial\chi^2/\partial\mathbf{r}_{n+1}(\mathbf{q})$ and $\partial\chi^2/\partial\mathbf{v}_{n+1/2}(\mathbf{q})$. We can use the chain rule to write $\partial\chi^2/\partial\mathbf{r}_n(\mathbf{q})$ and $\partial\chi^2/\partial\mathbf{v}_{n-1/2}(\mathbf{q})$ as

$$\frac{\partial\chi^2}{\partial\mathbf{v}_{n-1/2}(\mathbf{q})} = \sum_{\mathbf{q}_1}\left[\frac{\partial\mathbf{r}_{n+1}(\mathbf{q}_1)}{\partial\mathbf{v}_{n-1/2}(\mathbf{q})}\otimes\frac{\partial\chi^2}{\partial\mathbf{r}_{n+1}(\mathbf{q}_1)} + \frac{\partial\mathbf{v}_{n+1/2}(\mathbf{q}_1)}{\partial\mathbf{v}_{n-1/2}(\mathbf{q})}\otimes\frac{\partial\chi^2}{\partial\mathbf{v}_{n+1/2}(\mathbf{q}_1)}\right]\,, \qquad \text{(B3)}$$

$$\frac{\partial\chi^2}{\partial\mathbf{r}_n(\mathbf{q})} = \sum_{\mathbf{q}_1}\left[\frac{\partial\mathbf{r}_{n+1}(\mathbf{q}_1)}{\partial\mathbf{r}_n(\mathbf{q})}\otimes\frac{\partial\chi^2}{\partial\mathbf{r}_{n+1}(\mathbf{q}_1)} + \frac{\partial\mathbf{v}_{n+1/2}(\mathbf{q}_1)}{\partial\mathbf{r}_n(\mathbf{q})}\otimes\frac{\partial\chi^2}{\partial\mathbf{v}_{n+1/2}(\mathbf{q}_1)}\right]\,, \qquad \text{(B4)}$$

where the symbol $\otimes$ stands for matrix multiplication. According to the leapfrog equations (20) and (21) in the PM model, we have that

$$\frac{\partial\mathbf{r}_{n+1}(\mathbf{q}_1)}{\partial\mathbf{r}_n(\mathbf{q})} = \mathbf{I}\delta(\mathbf{q}_1 - \mathbf{q}) + \frac{\partial\mathbf{F}_n(\mathbf{r}_n(\mathbf{q}_1))}{\partial\mathbf{r}_n(\mathbf{q})}\Delta^{\rm v}_n\Delta^{\rm r}_n\,, \qquad \text{(B5)}$$

$$\frac{\partial\mathbf{r}_{n+1}(\mathbf{q}_1)}{\partial\mathbf{v}_{n-1/2}(\mathbf{q})} = \mathbf{I}\delta(\mathbf{q}_1 - \mathbf{q})\Delta^{\rm r}_n\,, \qquad \text{(B6)}$$

$$\frac{\partial\mathbf{v}_{n+1/2}(\mathbf{q}_1)}{\partial\mathbf{r}_n(\mathbf{q})} = \frac{\partial\mathbf{F}_n(\mathbf{r}_n(\mathbf{q}_1))}{\partial\mathbf{r}_n(\mathbf{q})}\Delta^{\rm v}_n\,, \qquad \text{(B7)}$$

$$\frac{\partial\mathbf{v}_{n+1/2}(\mathbf{q}_1)}{\partial\mathbf{v}_{n-1/2}(\mathbf{q})} = \mathbf{I}\delta(\mathbf{q}_1 - \mathbf{q})\,, \qquad \text{(B8)}$$

where $\mathbf{I}$ is a unit matrix, and $\delta(\mathbf{q}_1 - \mathbf{q})$ is equal to one when $\mathbf{q}_1 = \mathbf{q}$, and zero otherwise. In the derivation, we have used the facts that $\partial\mathbf{r}_n(\mathbf{q}_1)/\partial\mathbf{r}_n(\mathbf{q}) = \delta(\mathbf{q}_1 - \mathbf{q})\mathbf{I}$ and $\partial\mathbf{r}_n(\mathbf{q}_1)/\partial\mathbf{v}_{n-1/2}(\mathbf{q}) = 0$

Inserting these equations into equations (B3) and (B4), we obtain

$$\frac{\partial\chi^2}{\partial\mathbf{v}_{n-1/2}(\mathbf{q})} = \frac{\partial\chi^2}{\partial\mathbf{v}_{n+1/2}(\mathbf{q})} + \frac{\partial\chi^2}{\partial\mathbf{r}_{n+1}(\mathbf{q})}\Delta_n^{\rm r}\,, \tag{B9}$$

$$\frac{\partial\chi^2}{\partial\mathbf{r}_n(\mathbf{q})} = \frac{\partial\chi^2}{\partial\mathbf{r}_{n+1}(\mathbf{q})} + \Delta_n^{\rm v}\sum_{\mathbf{q}_1}\frac{\partial\mathbf{F}_n(\mathbf{r}_n(\mathbf{q}_1))}{\partial\mathbf{r}_n(\mathbf{q})}\otimes\frac{\partial\chi^2}{\partial\mathbf{v}_{n-1/2}(\mathbf{q}_1)} = \frac{\partial\chi^2}{\partial\mathbf{r}_{n+1}(\mathbf{q})} + \Delta_n^{\rm v}\mathbf{F}_n^{\chi}(\mathbf{q})\,. \tag{B10}$$

Using equation (25), the quantity $\mathbf{F}_n^{\chi}(\mathbf{q})$ defined in the second term can be written as

$$\begin{aligned}
\mathbf{F}_n^{\chi}(\mathbf{q}) &\equiv \sum_{\mathbf{q}_1}\frac{\partial\mathbf{F}_n(\mathbf{r}_n(\mathbf{q}_1))}{\partial\mathbf{r}_n(\mathbf{q})}\otimes\frac{\partial\chi^2}{\partial\mathbf{v}_{n-1/2}(\mathbf{q}_1)} \\
&= \sum_{\mathbf{q}_1}\sum_{\mathbf{x}_1} w_{\rm c}(\mathbf{x}_1-\mathbf{r}_n(\mathbf{q}_1))\frac{\partial\mathbf{F}_{{\rm g},n}(\mathbf{x}_1)}{\partial\mathbf{r}_n(\mathbf{q})}\otimes\frac{\partial\chi^2}{\partial\mathbf{v}_{n-1/2}(\mathbf{q}_1)} \\
&+ \sum_{\mathbf{q}_1}\sum_{\mathbf{x}_1}\frac{\partial w_{\rm c}(\mathbf{x}_1-\mathbf{r}_n(\mathbf{q}_1))}{\partial\mathbf{r}_n(\mathbf{q})}\left[\mathbf{F}_{{\rm g},n}(\mathbf{x}_1)\cdot\frac{\partial\chi^2}{\partial\mathbf{v}_{n-1/2}(\mathbf{q}_1)}\right] \\
&= \mathbf{F}_{n,a}^{\chi}(\mathbf{q}) + \mathbf{F}_{n,b}^{\chi}(\mathbf{q})\,,
\end{aligned} \tag{B11}$$

where '$\cdot$' stands for dot product, and the last line of the equation defines $\mathbf{F}_{n,a}^{\chi}(\mathbf{q})$ and $\mathbf{F}_{n,b}^{\chi}(\mathbf{q})$. The first term of $\mathbf{F}_n^{\chi}(\mathbf{q})$ can be rewritten as

$$\begin{aligned}
\mathbf{F}_{n,a}^{\chi}(\mathbf{q}) &\equiv \sum_{\mathbf{q}_1}\sum_{\mathbf{x}_1} w_{\rm c}(\mathbf{x}_1-\mathbf{r}_n(\mathbf{q}_1))\frac{\partial\mathbf{F}_{{\rm g},n}(\mathbf{x}_1)}{\partial\mathbf{r}_n(\mathbf{q})}\otimes\frac{\partial\chi^2}{\partial\mathbf{v}_{n-1/2}(\mathbf{q}_1)} \\
&= \sum_{\mathbf{x}_2}\frac{\partial\delta_{n,{\rm c}}(\mathbf{x}_2)}{\partial\mathbf{r}_n(\mathbf{q})}\sum_{\mathbf{k}}\frac{w_{\rm g}(R_{\rm PM}k)}{w_{\rm c}^2(\mathbf{k})N_c^3}{\rm e}^{-i\mathbf{k}\cdot\mathbf{x}_2}\frac{(i\mathbf{k}\cdot)}{k^2}\sum_{\mathbf{x}_1}{\rm e}^{i\mathbf{k}\cdot\mathbf{x}_1}\sum_{\mathbf{q}_1} w_{\rm c}(\mathbf{x}_1-\mathbf{r}_n(\mathbf{q}_1))\frac{\partial\chi^2}{\partial\mathbf{v}_{n-1/2}(\mathbf{q}_1)} \\
&= \sum_{\mathbf{x}_2}\sum_{\mathbf{q}_2}\frac{\partial w_{\rm c}(\mathbf{x}_2-\mathbf{r}_n(\mathbf{q}_2))}{\partial\mathbf{r}_n(\mathbf{q})}\sum_{\mathbf{k}}\frac{w_{\rm g}(R_{\rm PM}k)}{w_{\rm c}^2(\mathbf{k})N_c^3}{\rm e}^{-i\mathbf{k}\cdot\mathbf{x}_2}\frac{(i\mathbf{k}\cdot)}{k^2}\sum_{\mathbf{x}_1}{\rm e}^{i\mathbf{k}\cdot\mathbf{x}_1}\mathbf{d}_{v,n}(\mathbf{x}_1) \\
&= \sum_{\mathbf{x}_2}\frac{\partial w_{\rm c}(\mathbf{x}_2-\mathbf{r}_n(\mathbf{q}))}{\partial\mathbf{r}_n(\mathbf{q})}\sum_{\mathbf{k}}{\rm e}^{i\mathbf{k}\cdot(\mathbf{L}-\mathbf{x}_2)}\frac{w_{\rm g}(R_{\rm PM}k)}{w_{\rm c}^2(\mathbf{k})}\frac{(i\mathbf{k}\cdot\mathbf{d}_{v,n}^*(\mathbf{k}))}{k^2} \\
&= \sum_{\mathbf{x}_2}\frac{\partial w_{\rm c}(\mathbf{x}_2-\mathbf{r}_n(\mathbf{q}))}{\partial\mathbf{r}_n(\mathbf{q})}f_{v,n}(\mathbf{L}-\mathbf{x}_2)\,,
\end{aligned} \tag{B12}$$

where $f_{v,n}(\mathbf{L}-\mathbf{x}_2)$ is defined by the last line of the equation, and

$$\mathbf{d}_{v,n}(\mathbf{x}_1) \equiv \sum_{\mathbf{q}_1} w_{\rm c}(\mathbf{x}_1-\mathbf{r}_n(\mathbf{q}_1))\frac{\partial\chi^2}{\partial\mathbf{v}_{n-1/2}(\mathbf{q}_1)}\,. \tag{B13}$$

Thus, $\mathbf{d}_{v,n}(\mathbf{x}_1)$ is equivalent to CIC assignments of 'particles' located at $\mathbf{r}_n(\mathbf{q}_1)$ with 'masses' given by $\partial\chi^2/\partial\mathbf{v}_{n-1/2}(\mathbf{q}_1)$ to grid points. Its Fourier transform, $\mathbf{d}_{v,n}(\mathbf{k})$, can be obtained readily. Since $\partial w_{\rm c}(\mathbf{x}_2-\mathbf{r}_n(\mathbf{q}))/\partial\mathbf{r}_n(\mathbf{q})$ is nonzero only at a small number of grid cells close to $\mathbf{r}_n(\mathbf{q})$, the calculation

implied by the last line of equation (B12) is not time-consuming. The second term of $\mathbf{F}^{\chi}_{n}(\mathbf{q})$ can be rewritten as

$$\begin{aligned}\mathbf{F}^{\chi}_{n,b}(\mathbf{q}) &= \sum_{\mathbf{q}_1}\sum_{\mathbf{x}_1}\frac{\partial w_{\rm c}(\mathbf{x}_1-\mathbf{r}_n(\mathbf{q}_1))}{\partial \mathbf{r}_n(\mathbf{q})}\left[\mathbf{F}_{{\rm g},n}(\mathbf{x}_1)\cdot\frac{\partial\chi^2}{\partial\mathbf{v}_{n-1/2}(\mathbf{q}_1)}\right] \\ &= \sum_{\mathbf{x}_1}\frac{\partial w_{\rm c}(\mathbf{x}_1-\mathbf{r}_n(\mathbf{q}))}{\partial \mathbf{r}_n(\mathbf{q})}\left[\mathbf{F}_{{\rm g},n}(\mathbf{x}_1)\cdot\frac{\partial\chi^2}{\partial\mathbf{v}_{n-1/2}(\mathbf{q})}\right]. \qquad \text{(B14)}\end{aligned}$$

The above transformation can be carried out until $n = 0$ to give $\partial\chi^2/\partial\mathbf{r}_{\rm i}(\mathbf{q}) = \partial\chi^2/\partial\mathbf{r}_0(\mathbf{q})$ and $\partial\chi^2/\partial\mathbf{v}_{\rm i}(\mathbf{q}) = \partial\chi^2/\partial\mathbf{v}_0(\mathbf{q})$.

B.3. The Zel'dovich transformation

Finally, the likelihood term of the Hamiltonian force can be written as

$$F_j(\mathbf{k}) = \frac{\partial\chi^2}{\partial\delta_j(\mathbf{k})} = \sum_{\mathbf{q}}\left[\frac{\partial\chi^2}{\partial\mathbf{r}_{\rm i}(\mathbf{q})}\cdot\frac{\partial\mathbf{r}_{\rm i}(\mathbf{q})}{\partial\delta_j(\mathbf{k})} + \frac{\partial\chi^2}{\partial\mathbf{v}_{\rm i}(\mathbf{q})}\cdot\frac{\partial\mathbf{v}_{\rm i}(\mathbf{q})}{\partial\delta_j(\mathbf{k})}\right], \qquad \text{(B15)}$$

Inserting equations (12) and (13) into the above equation, we have

$$F_j(\mathbf{k}) = \sum_{\mathbf{q}}\frac{\partial\mathbf{s}(\mathbf{q})}{\partial\delta_j(\mathbf{k})}\cdot\left[\frac{\partial\chi^2}{\partial\mathbf{r}_{\rm i}(\mathbf{q})} + \frac{\partial\chi^2}{\partial\mathbf{v}_{\rm i}(\mathbf{q})}H_{\rm i}a_{\rm i}^2 f(\Omega_{\rm i})\right] = \frac{1}{N_{\rm c}^3}\sum_{\mathbf{q}}\frac{\partial\mathbf{s}(\mathbf{q})}{\partial\delta_j(\mathbf{k})}\cdot\mathbf{\Psi}(\mathbf{q})\,. \qquad \text{(B16)}$$

With the use of the Fourier transform of $\mathbf{s}(\mathbf{q})$ given in equation (14), the Hamiltonian force can be rewritten as,

$$F_j(\mathbf{k}) = \sum_{\mathbf{k}_1}\frac{D(a_{\rm i})}{k_1^2}\frac{\partial\delta(\mathbf{k}_1)}{\partial\delta_j(\mathbf{k})}(i\mathbf{k}_1\cdot)\frac{1}{N_{\rm c}^3}\sum_{\mathbf{q}}\mathbf{\Psi}(\mathbf{q})\mathrm{e}^{i\mathbf{k}_1\cdot\mathbf{q}} = \sum_{\mathbf{k}_1}\frac{D(a_{\rm i})}{k_1^2}\frac{\partial\delta(\mathbf{k}_1)}{\partial\delta_j(\mathbf{k})}(i\mathbf{k}_1\cdot\mathbf{\Psi}^*(\mathbf{k}_1))\,, \qquad \text{(B17)}$$

where $\mathbf{\Psi}(\mathbf{k}_1)$ is the Fourier transform of $\mathbf{\Psi}(\mathbf{q})$. Since $\partial\delta(\mathbf{k}_1)/\partial\delta_j(\mathbf{k})$ is nonzero only when $\mathbf{k}_1 = \pm\mathbf{k}$, we eventually obtain the expression of the likelihood term of the Hamiltonian force for the real part of $\delta(\mathbf{k})$ as

$$F_{\rm re}(\mathbf{k}) = \frac{2D(a_{\rm i})}{k^2}\mathbf{k}\cdot\mathbf{\Psi}_{\rm im}(\mathbf{k})\,, \qquad \text{(B18)}$$

and for the imaginary part as

$$F_{\rm im}(\mathbf{k}) = -\frac{2D(a_{\rm i})}{k^2}\mathbf{k}\cdot\mathbf{\Psi}_{\rm re}(\mathbf{k})\,, \qquad \text{(B19)}$$

where $\mathbf{\Psi}_{\rm re}(\mathbf{k})$ and $\mathbf{\Psi}_{\rm im}(\mathbf{k})$ are the real and imaginary parts of $\mathbf{\Psi}(\mathbf{k})$, respectively.

C. Test of the HMC+PM method using PM density fields as input

As shown in Section 4.2, there is always a small bump in the reconstructed linear power spectrum relative to the original one. There are two possibilities for this bias. One is the inaccuracy

of the adopted dynamical model, and the other is due to the HMC method itself. In order to distinguish these two possibilities, we apply the HMC method to density fields generated by the PM model, so that the first possibility is not an issue and any remaining bias should be due to the HMC method. Two PM density fields in periodic boxes of 300 and $100\,h^{-1}$Mpc are used for the test. The density field in the larger box is generated by using PM10, while the smaller box by using PM40. When applying our method to these PM density fields, exactly the same PM models are implemented in the HMC runs. Thus, the PM models adopted in these HMC runs can be regarded as 100 percent accurate.

Four HMC tests are performed . Two are applied to the PM10 density fields smoothed on scales of $R_{\rm s} = 4.5\,h^{-1}$Mpc and $3\,h^{-1}$Mpc, respectively. The other two use the PM40 density fields smoothed with $R_{\rm s} = 2.25\,h^{-1}$Mpc and $1.5\,h^{-1}$Mpc as inputs. Figure 16 shows the power spectrum ratio, $P_{\rm rc}(k)/P_{\rm lin}(k)$, where $P_{\rm rc}(k)$ is measured from the reconstructed linear density field and $P_{\rm lin}(k)$ is the original linear power spectrum. In each test, the power spectrum is well recovered on both large and small scales. However, there is a significant but weak (about 10%) dip in the power spectrum ratios. A clear trend is observed that the wavenumber where the dip appears (hereafter $k_{\rm d}$) increases with decreasing smoothing scale.

To understand the origin of this discrepancy, we show in the same figure the average ratio ($R_{\rm F}$) between the likelihood and prior terms of the Hamiltonian force. This ratio decreases monotonically with increasing k. More importantly, this ratio is about one at the scale $k_{\rm d}$ (see also the discussion in W13). This strongly suggests that the dip in the reconstructed linear power spectrum originates from the competition between the two Hamiltonian force terms. The Hamiltonian force is the most important quantity that drives the evolution of $\delta(\mathbf{k})$ in the fictitious system. At large scales where $R_{\rm F} \gg 1$, the trajectories of $\delta(\mathbf{k})$ are dominated by the likelihood term so that they eventually trace well the original linear density field. At small scales where $R_{\rm F} \ll 1$, on the other hand, the trajectories of $\delta(\mathbf{k})$ are governed by the prior term, so that the reconstructed power spectrum matches the original power spectrum but with totally unconstrained phases. On scales $R_{\rm F} \sim 1$, where the two terms have approximately the same importance, the compromise between them leads to the observed dip. Since the likelihood term increases with the decrease of the smoothing scale, $R_{\rm s}$, while the prior term does not, it explains why the dip moves towards smaller scales as $R_{\rm s}$ decreases.

The deviation observed in Section 4.2 also appears around the scale where $R_{\rm F} = 1$, indicative of the same origin. The question is why a bump appears in the applications to N-body simulations, while a dip is found here. This difference is clearly due to the inaccuracy of the PM model relative to the N-body simulation. An approximate model in general under-predicts the power spectrum at small scales. Although such bias is suppressed by smoothing (specified by $R_{\rm s}$), the reconstructed spectrum is still required to be enhanced by the HMC to compensate the under-prediction by the PM model. The use of a smaller smoothing scale can push the deviation to a smaller scale. Since $R_{\rm s} > 2l_{\rm c}$ is required (see Section 3.2), a smaller $R_{\rm s}$ therefore requires a smaller $l_{\rm c}$ and larger $N_{\rm PM}$.

REFERENCES

Ata M., Kitaura F.-S., Müller V., 2014, arXiv, arXiv:1406.7796

Bertschinger E., 1987, ApJ, 323, L103

Brenier Y., Frisch U., Hénon M., Loeper G., Matarrese S., Mohayaee R., Sobolevskiĭ A., 2003, MNRAS, 346, 501

Carlstrom J. E., Holder G. P., Reese E. D., 2002, ARA&A, 40, 643

Caucci S., Colombi S., Pichon C., Rollinde E., Petitjean P., Sousbie T., 2008, MNRAS, 386, 211

Davis M., Efstathiou G., Frenk C. S., White S. D. M., 1985, ApJ, 292, 371

Doumler T., Hoffman Y., Courtois H., Gottlöber S., 2013, MNRAS, 430, 888

Duane S., Kennedy A. D., Pendleton B. J., Roweth D., 1987, PhLB, 195, 216

Eisenstein D. J., Hu W., 1998, ApJ, 496, 605

Fang T., Marshall H. L., Lee J. C., Davis D. S., Canizares C. R., 2002, ApJ, 572, L127

Frisch U., Matarrese S., Mohayaee R., Sobolevski A., 2002, Natur, 417, 260

Giovanelli R., et al., 2005, AJ, 130, 2598

Gottloeber S., Hoffman Y., Yepes G., 2010, arXiv, arXiv:1005.2687

Hajian A., 2007, PhRvD, 75, 083525

Hanson K. M., 2001, "Markov Chain Monte Carlo posterior sampling with the Hamiltonian method," in Medical Imaging: Image Processing, M. Sonka and K. M. Hanson, eds., Proc. SPIE 4322, pp. 456-467

Hanson K. M., Cunningham, G. C., 1996, "A computationalapproach to Bayesian inference," in Computing Science and Statistics 27, M. M. Meyer and J. L. Rosenberger, eds., pp. 202-211, Interface Foundation, Fairfax Station, VA 22039-7460

Heß S., Kitaura F.-S., Gottlöber S., 2013, MNRAS, 435, 2065

Hockney R. W., Eastwood J. W., 1981, Computer Simulation Using Particles (New York: McGraw-Hill)

Hoffman Y., Ribak E., 1991, ApJ, 380, L5

Jasche J., Kitaura F. S., 2010, MNRAS, 407, 29

Jasche J., Wandelt B. D., 2013, MNRAS, 432, 894

Jing Y. P., Suto Y., 2002, ApJ, 574, 538

Kitaura F. S., Enßlin T. A., 2008, MNRAS, 389, 497

Kitaura F.-S., Gallerani S., Ferrara A., 2012, MNRAS, 420, 61

Kitaura F.-S., 2013, MNRAS, 429, L84

Kitaura F.-S., Heß S., 2013, MNRAS, 435, L7

Klypin A., Hoffman Y., Kravtsov A. V., Gottlöber S., 2003, ApJ, 596, 19

Klypin A. A., Shandarin S. F., 1983, MNRAS, 204, 891

Kolatt T., Dekel A., Ganon G., Willick J. A., 1996, ApJ, 458, 419

Koribalski B. S., et al., 2004, AJ, 128, 16

Kravtsov A. V., Klypin A., Hoffman Y., 2002, ApJ, 571, 563

Lavaux G., 2010, MNRAS, 406, 1007

Lee K.-G., Hennawi J. F., White M., Croft R. A. C., Ozbek M., 2014, ApJ, 788, 49

Mo H., van den Bosch F. C., White S., 2010, Galaxy Formation and Evolution (Cambridge: Cambride University Press).

Muñoz-Cuartas J. C., Müller V., Forero-Romero J. E., 2011, MNRAS, 417, 1303

Neal R., 1993, Bayesian Learning for Neural Networks (Springer:New York)

Nusser A., Dekel A., 1992, ApJ, 391, 443

Peebles P. J. E., 1989, ApJ, 344, L53

Pichon C., Vergely J. L., Rollinde E., Colombi S., Petitjean P., 2001, MNRAS, 326, 597

Saintonge A., et al., 2011, MNRAS, 415, 32

Savage B. D., Tripp T. M., Lu L., 1998, AJ, 115, 436

Springob C. M., Haynes M. P., Giovanelli R., Kent B. R., 2005, ApJS, 160, 149

Schaap W. E., van de Weygaert R., 2000, A&A, 363, L29

Sheth R. K., Mo H. J., Tormen G., 2001, MNRAS, 323, 1

Springel V., 2005, MNRAS, 364, 1105

Tassev S., Zaldarriaga M., 2012a, JCAP, 4, 13

Tassev S., Zaldarriaga M., 2012b, JCAP, 12, 11(TZ12)

Taylor J. F., Ashdown M. A. J., Hobson M. P., 2008, MNRAS, 389, 1284

van de Weygaert R., Bertschinger E., 1996, MNRAS, 281, 84

Wang H., Mo H. J., Jing Y. P., Guo Y., van den Bosch F. C., Yang X., 2009a, MNRAS, 394, 398

Wang H., Mo H. J., Jing Y. P., Yang X., Wang Y., 2011, MNRAS, 413, 1973

Wang H., Mo H. J., Yang X., van den Bosch F. C., 2012, MNRAS, 420, 1809

Wang H., Mo H. J., Yang X., van den Bosch F. C., 2013, ApJ, 772, 63 (W13)

Warren M. S., Abazajian K., Holz D. E., Teodoro L., 2006, ApJ, 646, 881

Werk J. K., Prochaska J. X., Thom C., Tumlinson J., Tripp T. M., O'Meara J. M., Peeples M. S., 2013, ApJS, 204, 17

White S. D. M., Frenk C. S., Davis M., 1983, ApJ, 274, L1

Yang X., Mo H. J., van den Bosch F. C., Pasquali A., Li C., Barden M., 2007, ApJ, 671, 153

York D. G., et al., 2000, AJ, 120, 1579

Young J. S., et al., 1995, ApJS, 98, 219

Zaroubi S., Hoffman Y., Fisher K. B., Lahav O., 1995, ApJ, 449, 446

Zel'dovich Y. B., 1970, A&A, 5, 84

This preprint was prepared with the AAS LaTeX macros v5.2.

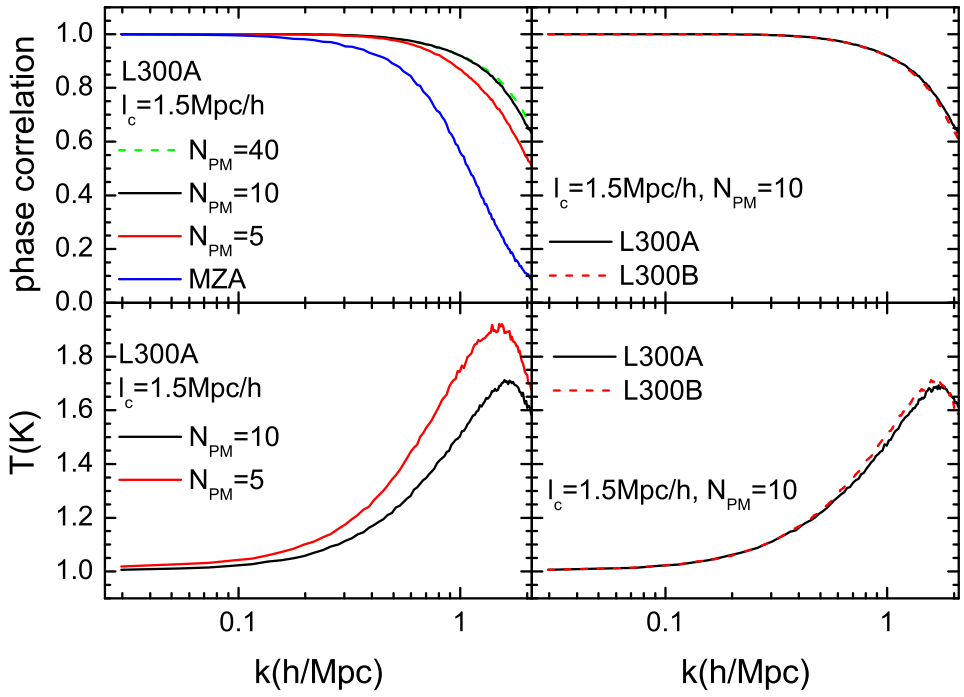

Fig. 1.— Upper left panel: the phase correlations between N-body simulated density field (L300A) and various modeled density fields as indicated in the panel. Here $N_{\rm PM}$ is the number of steps adopted in a PM model and $l_{\rm c}$ is the grid cell size. Upper right panel: the phase correlations between the simulated density fields and the corresponding PM density fields with $N_{\rm PM} = 10$. Lower left panel: the density transfer functions for PM models with $N_{\rm PM} = 5$ and 10. Lower right panel: density transfer functions for PM model with $N_{\rm PM} = 10$, derived from two simulations. The grid cell size is set to $1.5\,h^{-1}$Mpc for all cases.

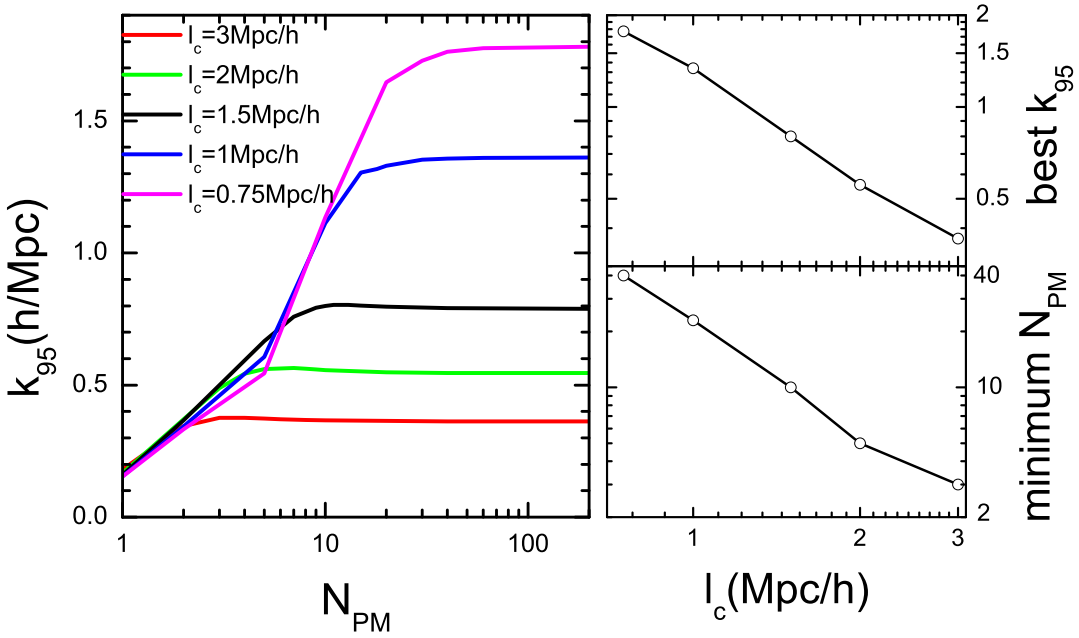

Fig. 2.— Left panel: the parameter k_{95} as a function of $N_{\rm PM}$ for different grid cell sizes, $l_{\rm c}$, as indicated in the figure. Here k_{95} measures the scale at which the phase correlation between the PM density field and the original simulated density field is 0.95. Right panels: the best k_{95} and the required minimum $N_{\rm PM}$ as a function of $l_{\rm c}$. All of the results are based on the simulation L300A.

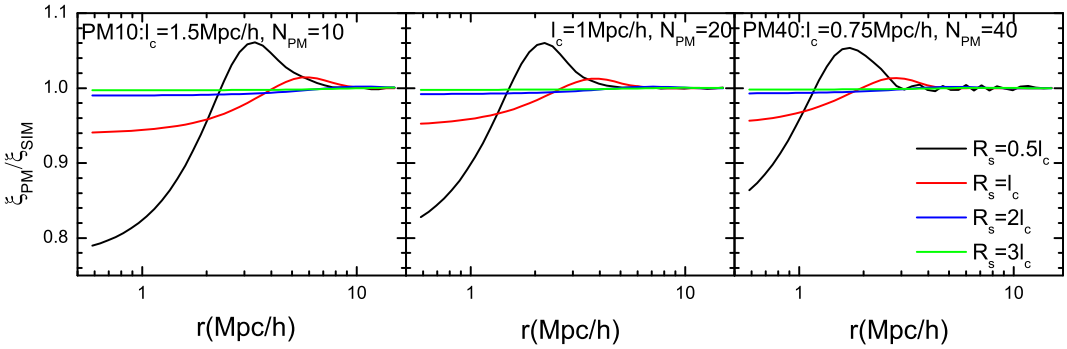

Fig. 3.— The ratios between the two-point correlation functions measured from the PM and the simulated density fields for three PM models as indicated in the panels. The density fields are smoothed with various smoothing scales, $R_{\rm s}$, as indicated.

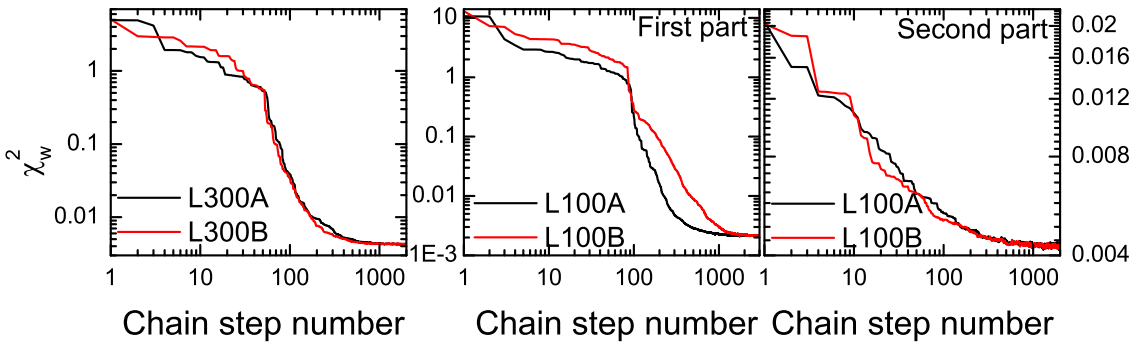

Fig. 4.— $\chi^2_w = \chi^2 / \sum_{\mathbf{x}} w(\mathbf{x})$ as a function of chain step for four HMC reconstructions. The left panel shows the results for the L300 series, while the middle and right panels show the results for the first and second HMC parts for the L100 series. The first HMC part adopts a larger smoothing scale than the second part.

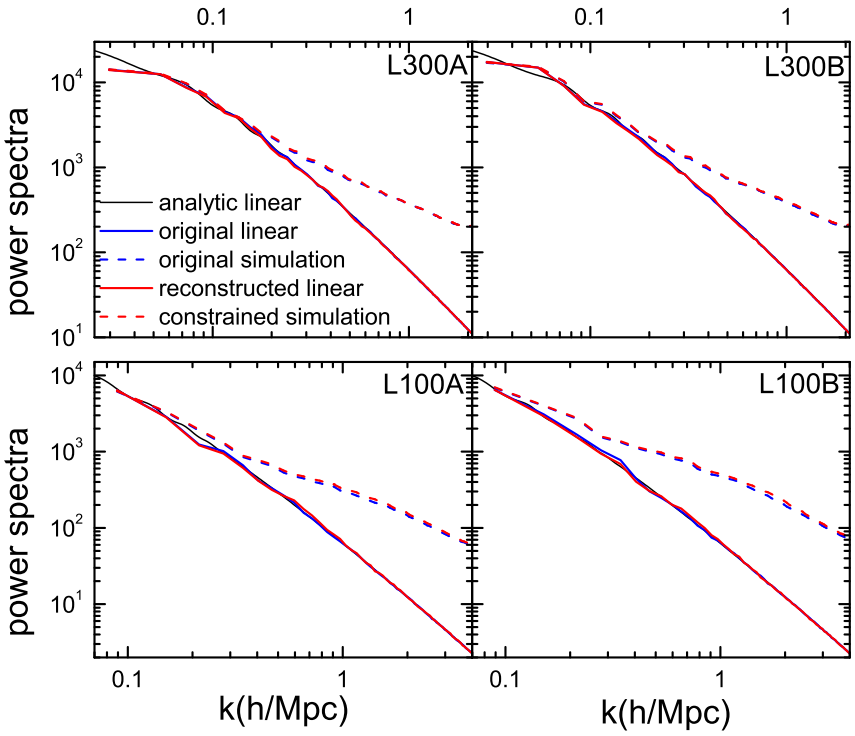

Fig. 5.— The blue and red solid lines show the original and reconstructed linear power spectra. The blue and red dashed lines show the $z = 0$ power spectra measured from the original input simulations and corresponding CSs. The black solid lines show the analytic linear power spectrum.

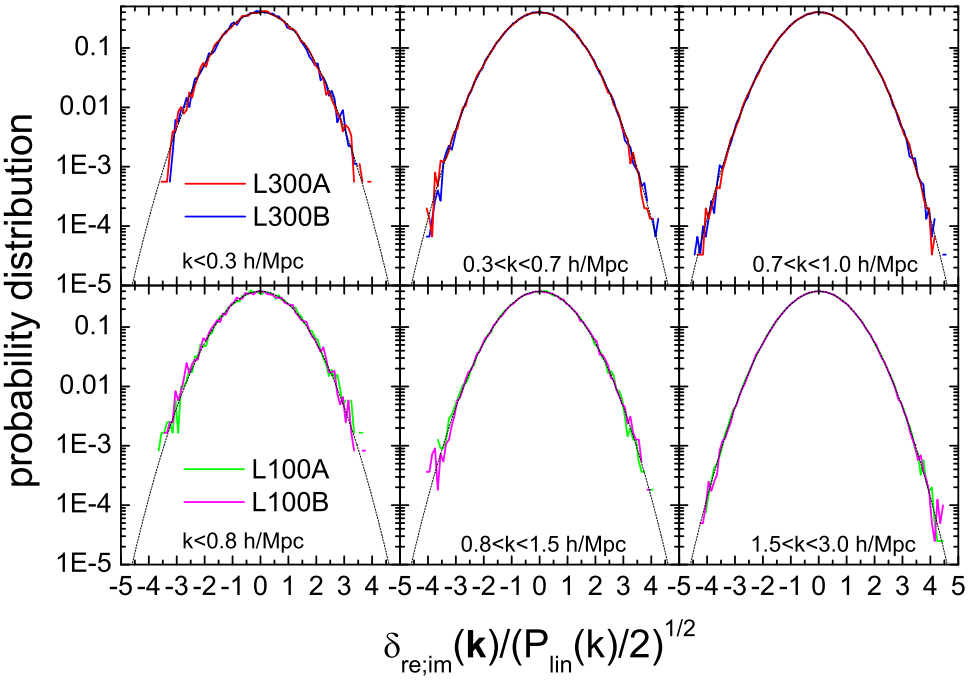

Fig. 6.— The distributions of $\delta_j(\mathbf{k})/\sqrt{P_{\rm lin}(k)/2}$ at three different scales as indicated in the panels. Here $\delta(\mathbf{k})$ is the reconstructed linear density field. The smooth curves are Gaussian distributions with dispersion $\sigma = 1$.

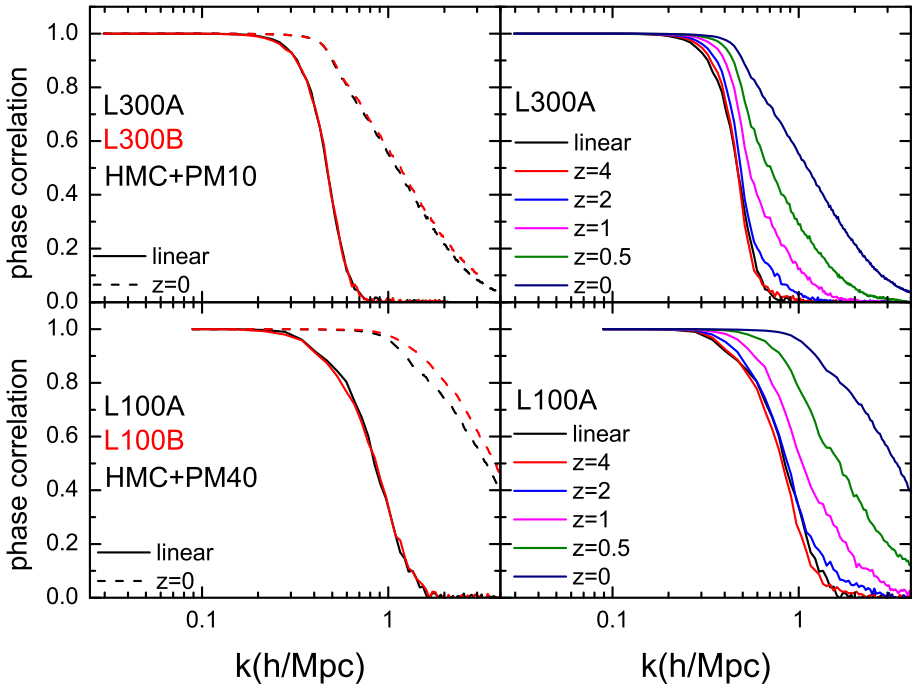

Fig. 7.— Left panels: the solid lines are the phase correlations between the original and reconstructed linear density fields, while the dashed lines are the phase correlations between the original (input) simulations and the corresponding CSs at redshift zero. Right panels: the phase correlations between the original simulation and the CS at various redshifts. The black line is the correlations of the linear density fields.

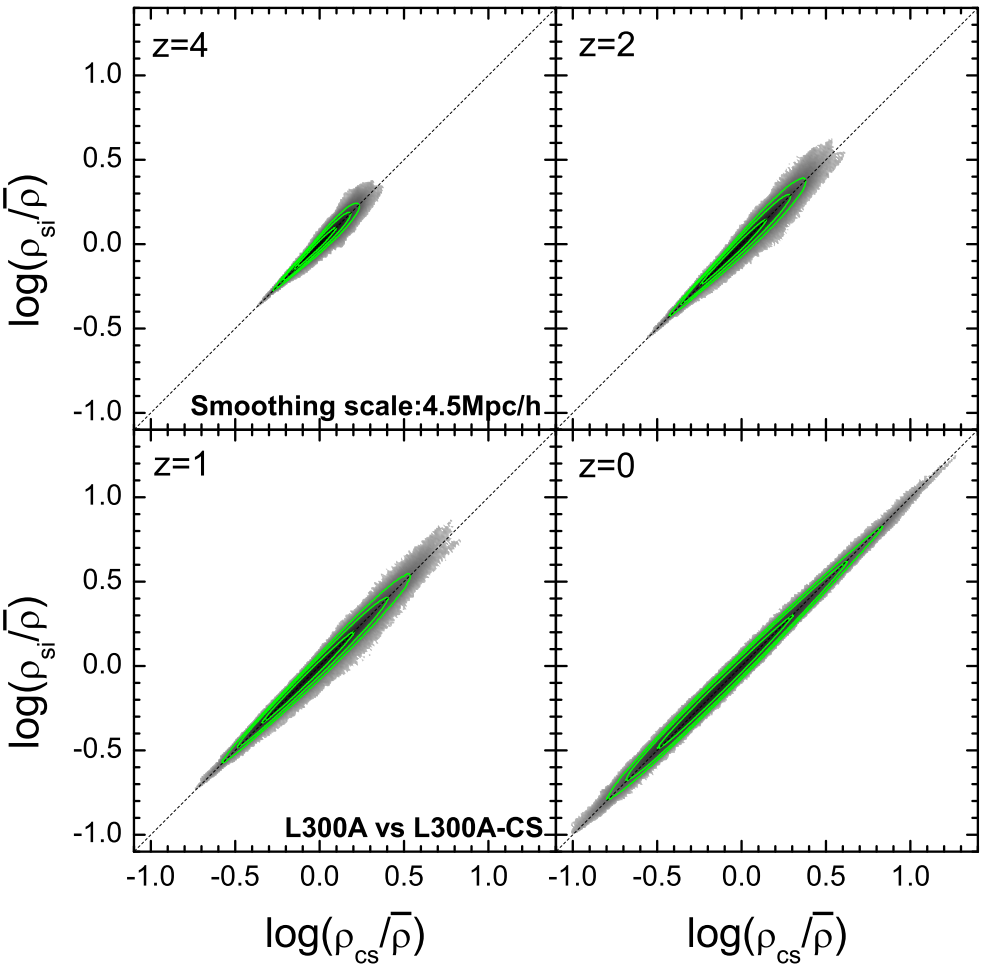

Fig. 8.— The density-density plots between the original simulation, L300A, and the corresponding CS at various redshifts. The density fields are smoothed with a Gaussian of radius $3\,h^{-1}$Mpc. The three contours encompass 67%, 95% and 99% of all the grid cells in the simulation box. All these densities are scaled with $\bar{\rho}$, the mean density of the universe at the redshift in question.

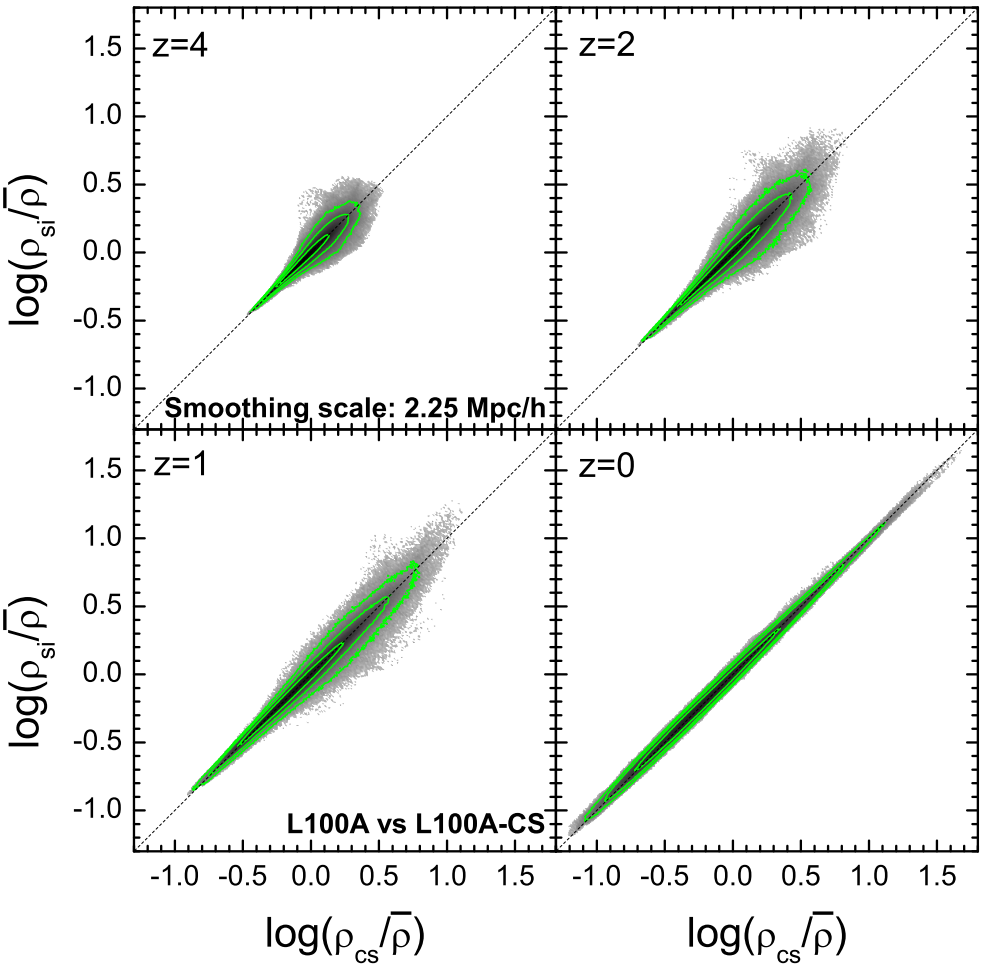

Fig. 9.— The same as Figure 8 but here for the L100A and its CS filtered with a Gaussian function of smaller radius $2.25\,h^{-1}$Mpc.

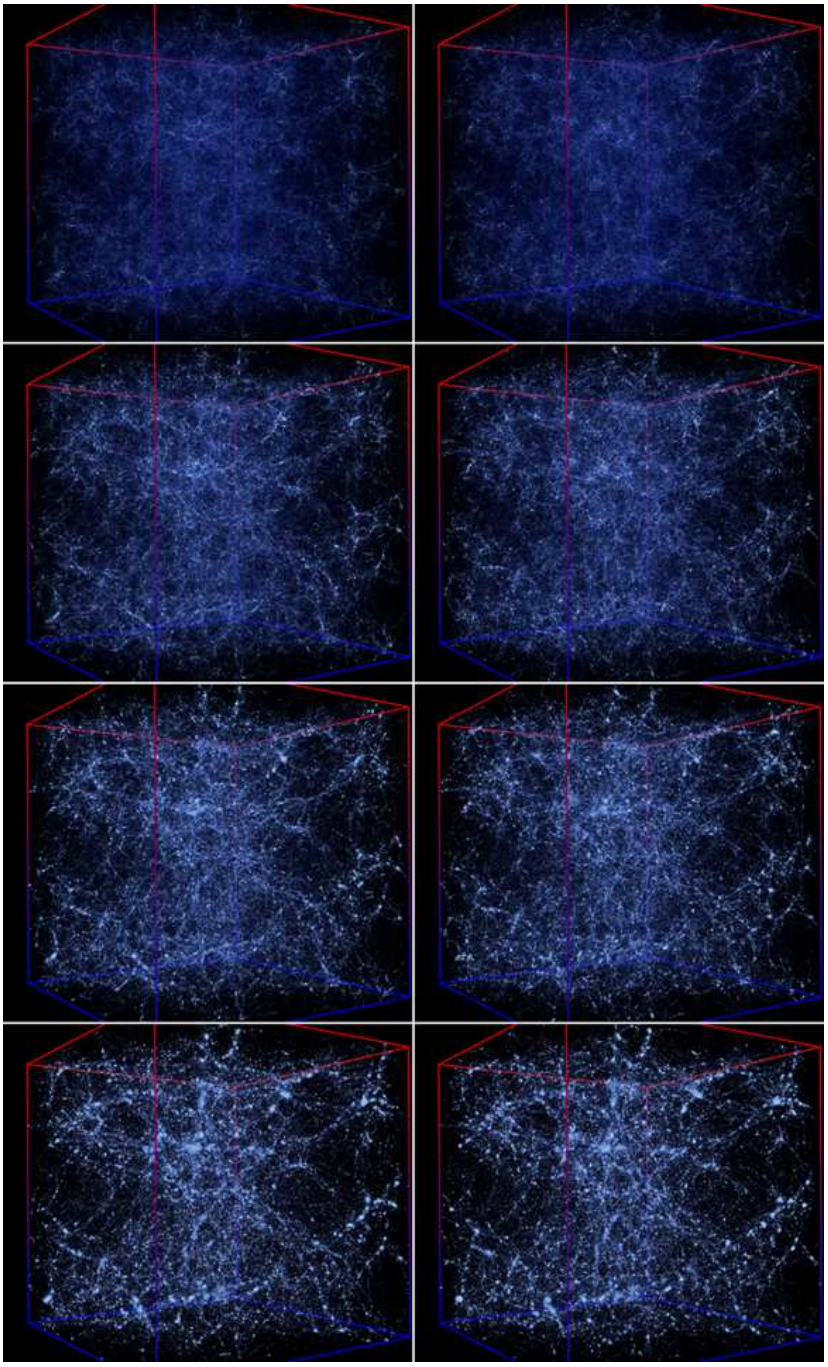

Fig. 10.— The 3-d renderings of the particle distributions, color-coded by density, in a cubic $100\,h^{-1}$Mpc box. The left panels show the particles in the simulation L100A and the right panels show those in the corresponding L100A-CS. The panels (from top to bottom) show the results at $z = 4$, 2, 1 and 0, respectively.

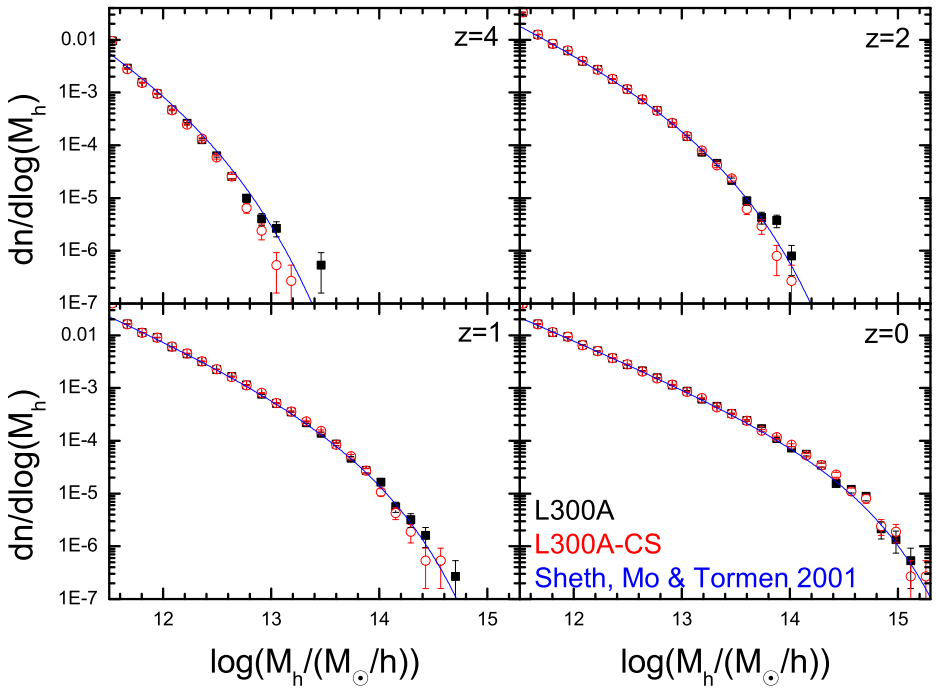

Fig. 11.— Halo mass functions obtained from L300A (squares) and L300A-CS (red circles) at four different redshifts. The blue lines represent the theoretical predictions (Sheth, Mo, & Tormen 2001).

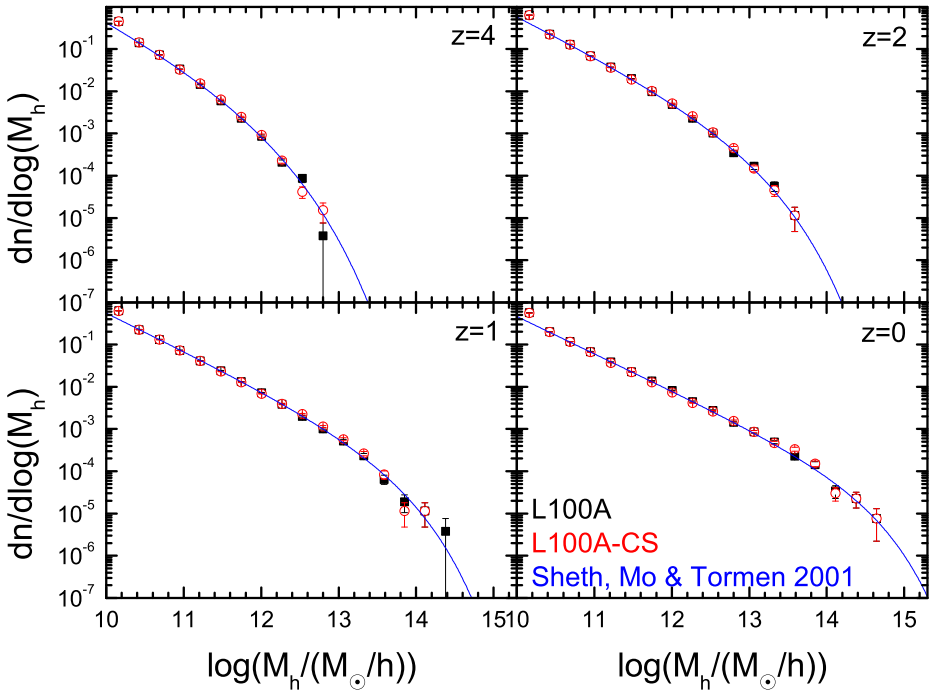

Fig. 12.— The same as Figure 11 but here for L100A and L100A-CS.

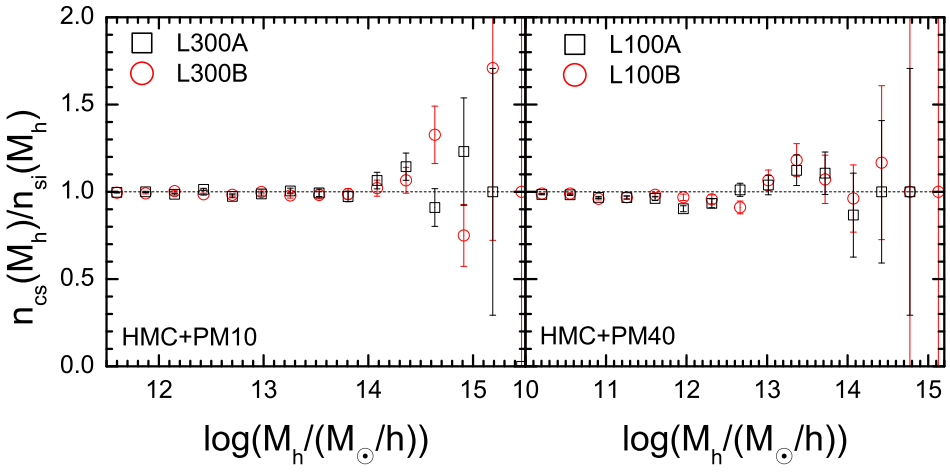

Fig. 13.— The ratio between the halo mass function obtained from the CS, $n_{\rm cs}$, and that from the original simulation, $n_{\rm si}$.

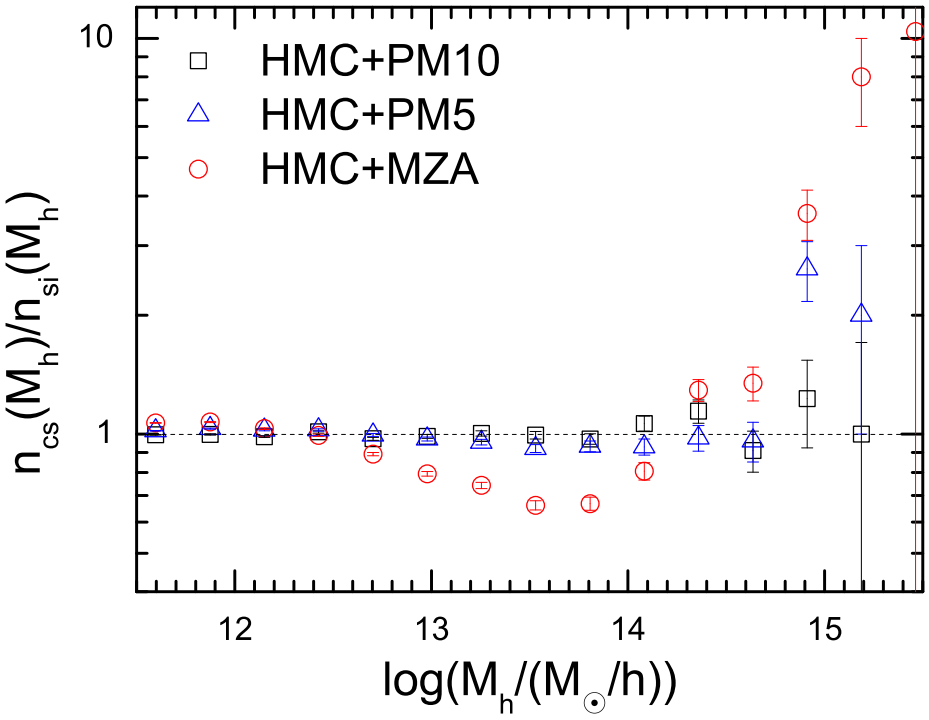

Fig. 14.— The ratio between the halo mass function derived from the reconstructed final density field and that from the original density field. Results are shown for different models of structure evolution, as indicated in the figure. The results are all based on L300A.

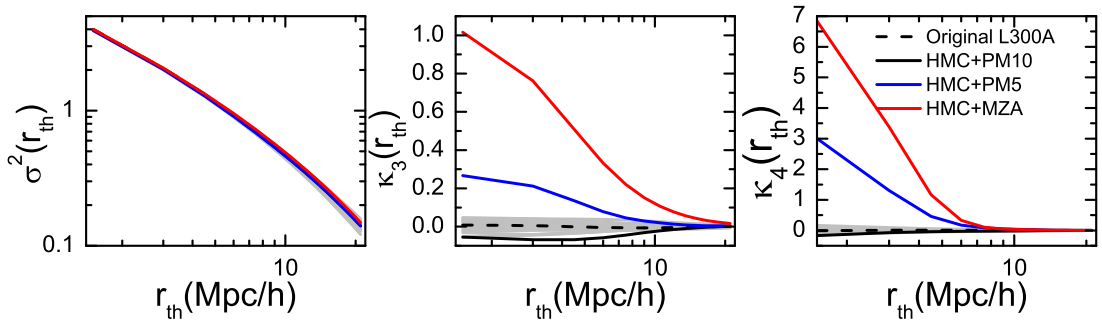

Fig. 15.— The variance (σ^2), skewness (κ_3) and kurtosis (κ_4) of the linear density fields in real space as a function of smoothing scale $r_{\rm th}$ (top-hat smoothing kernel). The black dashed lines show the results measured from the original linear density field of L300A. The solid lines show the results measured from the reconstructed linear density fields based on different models of structure evolution, as indicated in the right panel. The grey bands show the spread of 19 linear density fields randomly sampled from the prior Gaussian distribution, $G(\delta(\mathbf{k}))$, given in equation (1).

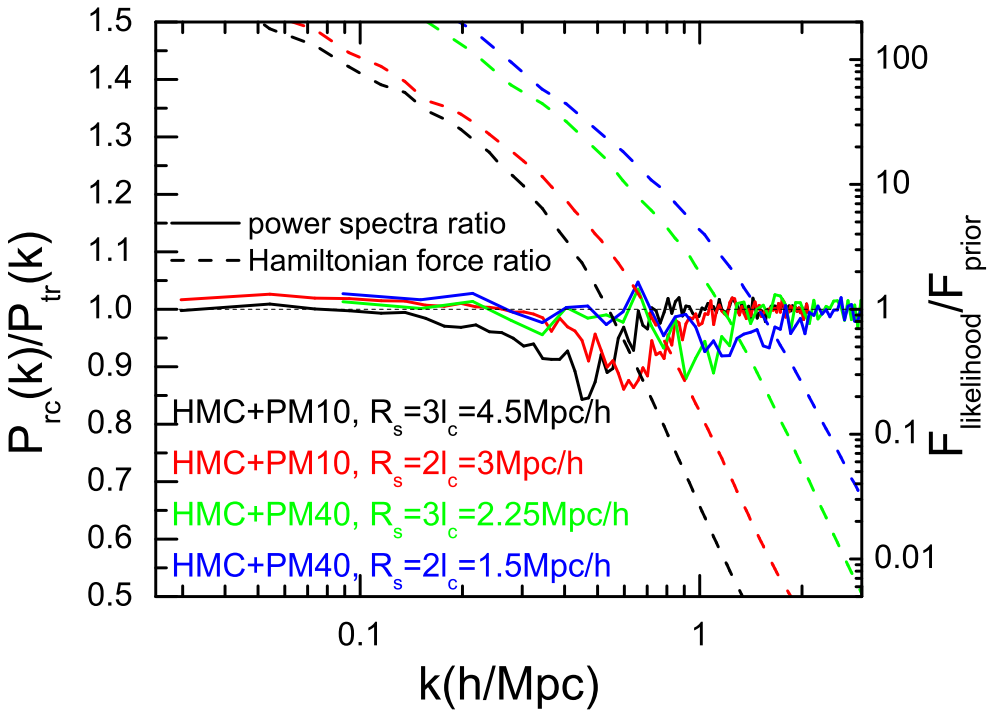

Fig. 16.— The solid lines show the reconstructed linear power spectra, normalized by the true power spectrum (left axis), $P_{\rm rc}/P_{\rm tr}$. The dashed lines show the ratios between the likelihood term and prior term of the Hamiltonian force (right axis). These reconstructions are for PM density fields as input, as detailed in Appendix C.